ISSN: 2164-5388 Volume 9, Number 4, October 2019

Scientific Research Publishing

Open Journal of Biophysics

ISSN: 2164-5388

https://www.scirp.org/journal/ojbiphy

Journal Editorial Board

ISSN Print: 2164-5388 ISSN Online: 2164-5396
https://www.scirp.org/journal/ojbiphy

Associate Editors

Editorial Board

Scientific Research Publishing

Open Journal of Biophysics, 2019, 9, 239-275
https://www.scirp.org/journal/ojbiphy
ISSN Online: 2164-5396
ISSN Print: 2164-5388

Table of Contents

Volume 9 Number 4 October 2019

Open Journal of Biophysics (OJBIPHY)
Journal Information

SUBSCRIPTIONS

The *Open Journal of Biophysics* (Online at Scientific Research Publishing, https://www.scirp.org/) is published quarterly by Scientific Research Publishing, Inc., USA.

Subscription rates:
Print: $79 per issue.
To subscribe, please contact Journals Subscriptions Department, E-mail: sub@scirp.org

SERVICES

Advertisements
Advertisement Sales Department, E-mail: service@scirp.org

Reprints (minimum quantity 100 copies)
Reprints Co-ordinator, Scientific Research Publishing, Inc., USA.
E-mail: sub@scirp.org

COPYRIGHT

PRODUCTION INFORMATION

For manuscripts that have been accepted for publication, please contact:
E-mail: ojbiphy@scirp.org

Scientific Research Publishing

Open Journal of Biophysics, 2019, 9, 239-253
https://www.scirp.org/journal/ojbiphy
ISSN Online: 2164-5396
ISSN Print: 2164-5388

ISFET Based DNA Sensor: Current-Voltage Characteristic and Sensitivity to DNA Molecules

Lusine Gasparyan[1,2], Ilya Mazo[1], Vahan Simonyan[3], Ferdinand Gasparyan[1,2]

[1]Argentis LLC, Gaithersburg, MD, USA
[2]Yerevan State University, Yerevan, Armenia
[3]The Department of Biochemistry & Molecular Medicine, The George Washington University, Washington DC, USA
Email: fgaspar@ysu.am

How to cite this paper: Gasparyan, L., Mazo, I., Simonyan, V. and Gasparyan, F. (2019) ISFET Based DNA Sensor: Current-Voltage Characteristic and Sensitivity to DNA Molecules. *Open Journal of Biophysics*, **9**, 239-253.
https://doi.org/10.4236/ojbiphy.2019.94017

Received: August 7, 2019
Accepted: August 24, 2019
Published: August 27, 2019

Abstract

Dependency of both source-drain current and current sensitivity of nanosize ISFET biosensor vs. concentration of DNA molecules in aqueous solution theoretically is investigated. In calculations it is carried out effects concerning charge carriers distribution in current channel and concerning carriers' mobility behavior in high electrical fields in the channel. The influence of DNA molecules on the work of ISFET biosensors is manifested by a change in the magnitude of the gate surface charge. Starting with fairly low concentrations of DNA, ISFET sensors respond to the presence of DNA molecules in an aqueous solution which is manifested by modulation of channel conductance and therefore the source-drain current changes of the field-effect transistor. It is shown that the current sensitivity with respect to concentration of DNA molecules linearly depends on the source-drain voltage and reaches high values.

Keywords

DNA, ISFET, Sensitivity, Nanosize, Current Channel

1. Introduction

The ion-sensitive field-effect transistor (ISFET) is one of the most popular semiconductor biosensors, and has been introduced as the first nanosized bio-chemical sensor. Currently, the use of ISFET technology encompasses a wide range of applications in a variety of areas, and those in the bioelectronic monitoring areas are particularly noteworthy. The ISFET sensor has been used to measure H^+ or OH^- ions concentrations in aqueous solution, causing an interface potential on the gate insulator (oxide). Much attention has been paid to silicon based bio-

sensors in the field of bio-analytical applications due to their favorable characteristics (Si-based technology, sensitivity, speed, signal-to-noise ratio, miniaturization, etc.). The introduction of the ISFET biosensor was in 1970 [1]; the first report regarding the use of an enzymatically modified ISFET for the direct detection of penicillin was in 1980 [2]. The operating principle of the ISFET device and recent advances and developments in the bio-analytical use of ISFET-based biosensors and detection strategies were covered in reviews [3] [4] [5]. Label-free detection of DNA using field-effect transistors (FET) with a real-time electrical readout system for rapid, cost-effective, and simple analysis of DNA samples has been proposed in [6]. When DNA strands bind to the free sites of gate surface of ISFETs, changes in surface electrical potential occur due to the negative charge of DNA molecule, shift in the source-drain current-voltage or capacitance-voltage characteristics thereby allowing for excellent performance of DNA sensing. Then conductivity of the semiconductor depletion layer will be modulated and source-drain signal current will be changed. It is clear that the capacitance of the system electrolyte-insulator-semiconductor depletion layer will be changed. In [7] DNA binding behavior was monitored using an ISFET biosensor, which was observed as changes in the threshold voltage. The change in DNA architecture and content, either due to hybridization or enzymatic reaction, yields a local pH charge variation and a rearrangement of ionic species near the sensor surface that modulate the sensor's response. One of the main disadvantages in measuring the biomolecular recognition using FET-biosensors is the Debye screening length. For this reason, it is necessary for FET measurements that biological sensing should take place within the Debye length. Field-effect transistors are described as three-electrode devices in which the current flowing between the source and drain electrodes can be modulated by changing the potential applied to the gate and source electrodes [8]. The current-control mechanism is based on an electric field generated by the voltage applied to the gate layer [8]. The current is conducted by one type of carriers (electrons or holes) depending on the semiconductor type. In the case of a p-type semiconductor, when a positive gate voltage is applied, holes are repelled from the semiconductor-insulator interface creating a depletion layer. Applying a positive gate voltage attracts electrons to the semiconductor surface, when a sufficiently high concentration of electrons is accumulated in this region a conductive channel is created at the semiconductor-insulator interface allowing a current flow between source and drain. The gate voltage modulates the channel conductance. Some groups reported on the use of FETs for real-time amplification and detection of nucleic acid using pH sensing [9] [10] [11] [12]. Detail review of advances and developments in the bio-analytical use of ISFET-based biosensors presented in [3] [5]. An electrochemical sensor for detection of unlabeled ssDNA using peptide nucleic acid probes coupled to the FET gate is demonstrated in [13]. An application of ISFET technology for the detection of single nucleotide polymorphisms suggested in [14]. In this study authors developed a useful procedure for sequencing one base via the detection of single-base mismatch in DNA. Note that

the sequencing mechanisms of sensors based on ISFETs can actually be used only for detecting nucleic acid using pH sensitivity and amplifying the useful signal in real time. Static, dynamic characteristics and pH sensitivity of bio FET sensors made on nanosize silicon (nanowire, nanoribbon) are detailed study by us in [15] [16] [17]. In [17] pH sensitivity of the biochemical sensors was introduced as $\Delta I_{ds}/\Delta\text{pH}$, where, ΔI_{ds} and ΔpH are the elementary changes in source-drain current and pH. Current-voltage characteristics, low-frequency noises, pH-sensitivity and SNR (signal-to-noise ratio) for liquid and back double gated Si NW (nanowire) sensors are investigated. It is shown that source-drain current substantially depends on pH-value and grows with increasing of the liquid gate voltage. The pH sensitivity increases as a result of the liquid gate voltage increase, giving opportunity to measure very low proton concentrations in the electrolyte medium at the high values of the front gate voltage. It is shown that SNR for Si NW based biochemical sensor has higher value, reaching up to 10^5. In [15] [16] it is shown that in Si nanosize FET biosensors pH sensitivity increases with the increase of current channel length approaching the Nernst limit value of 59.5 mV/pH, indicating that larger area devices are more suitable for the pH sensing. The pH sensitivity increases also with the increasing of the back-gate voltage and approaches to 59.5 mV/pH.

The analysis conducted above shows a high level of experimental research in this area. Very good results have been achieved in the field of sensors fabrication and pH-sensitivity; effective methods have been proposed for lowering the level of low-frequency noise in order to increase the signal-to-noise ratio. However, it seems to us that there are still many open questions when studying the physical mechanisms occurring in a semiconductor and interface semiconductor-insulator that determine and influence on the basic parameters of the sensors.

The aim of this research is the theoretical investigation, simulation and demonstration of the dependency of source-drain current of the silicon nanowire based ISFET biosensor vs. concentration of DNA molecules in aqueous solution. DNA detection mechanism and source-drain current sensitivity depending on the influence of the DNA molecules which occur in an aqueous solution over the Debye screening length will be investigated and discussed.

2. Physical Processes in the ISFET Biosensor

To study the source-drain current of the ISFET biosensor and its sensitivity to the presence of negatively charged DNA molecules in an aqueous solution, it is necessary to consider the physical processes occurring, in particular, at the interface between the gate insulator and the electrolyte. The main physical processes taking place in the ISFET biosensor for DNA molecule detection are sketched in **Figure 1**. It is presented a schematic representation of the device structure (a), distribution of the gate potential V_g over the layered structure of the biosensor (b), and energy diagram of the electrolyte-insulator-semiconductor structure. In the left side of **Figure 1** also shows the coordinate system used.

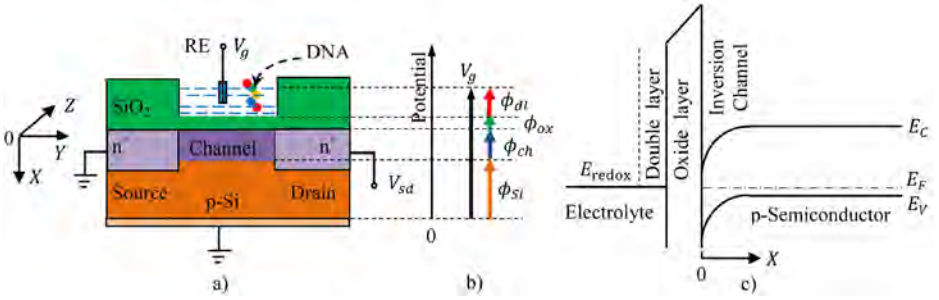

Figure 1. Schematic illustration of the ISFET biosensor (a), distribution of potentials (b), and energy diagram of ISFET in equilibrium ($V_g = 0$) (c). Here RE means reference electrode; V_g is the gate voltage, V_{sd} is the source-drain potential, E_F is the semiconductor Fermi level energy, E_C is the conduction and E_V is the valence band energy, E_{redox} is the redox potential. The colored circles in figure (a) show the DNA nucleotides adenine, thymine, guanine and cytosine.

Particularly silicon based structures and silicon oxide as an insulator will be discussed. In the **Figure 1** RE is the reference electrode, V_g is the applied gate voltage, ϕ_{Si}, ϕ_{ch}, ϕ_{ox} and ϕ_{dl} are potentials of the silicon substrate, current channel (semiconductor depletion layer), oxide layer and double layer, correspondingly.

The balance equation for the potentials according to **Figure 1**, can be represented as follows:

$$V_g = \phi_s + \phi_{Si} + \phi_{ch} + \phi_{ox} + \phi_{dl}\,. \tag{1}$$

To estimate these potentials as well as the threshold voltage, V_{th}, and flat-band voltage, V_{FB}, we can use the following relations [8] [18]-[23]:

$$\begin{aligned} &V_{th} = V_{FB} + 2\varphi_F + \phi_{ch};\ V_{FB} = \phi_{bulk,sol} - \phi_{ch} + \phi_{dl} - \frac{\Phi_{Si} - \Phi_{ox}}{q} + \frac{Q_{ox}}{C_{ox}};\\ &\phi_{bulk,sol} \approx 0;\ \phi_{Si} = \phi_{bulk,Si} \approx 0;\ \varphi_F = 2\varphi_T \ln\frac{N_A}{n_i};\ \phi_{ch} = \sqrt{\frac{4q\varepsilon_0\varepsilon_{Si}N_A\varphi_T}{C_{ox}^2}};\\ &\varphi_T = \frac{k_B T}{q};\ \phi_{dl} = 2\varphi_T\left(\frac{\varepsilon_w}{\varepsilon_r}\frac{N_{sol}}{K_{AK}^+ + H_s^+}\right);\ \phi_{ox} = \frac{qN_t}{C_{ox}}. \end{aligned} \tag{2}$$

Here q is the elementary charge; k_B is the Boltzmann's constant; T is the absolute temperature; φ_T is the thermal voltage; φ_F is the Fermi potential; $\phi_{bulk,sol}$ and $\phi_{bulk,Si}$ are the electric potentials of the bulk solution and the bulk silicon substrate; ϕ_{dl} is the potential of double layer; Φ_{Si} and Φ_{ox} are the work functions of silicon and silicon oxide (SiO_2), correspondingly; Q_{ox} is the oxide layer charge per unit area, C_{ox} is the capacitance of the oxide layer per unit area; ε_0, ε_{Si}, ε_{ox}, ε_w and ε_r are the dielectric permittivities of free space, silicon, silicon dioxide, water and electrolyte, respectively; N_A is the doping acceptor concentration in p-Si substrate; n_i is the intrinsic carrier concentration in bulk silicon; K_{AK}^+ is the molar concentration of the cations in the solution, H_s^+ is the molar concentration of the hydrogen ions at the oxide surface; N_{sol} is the molar concentration of the solution; N_t is the concentration

of surface open electronic binding sites (traps) per oxide unit area. Note that the redox potential E_{redox} is a measure of the ease with which a molecule will accept electrons and double layer in solution consist of IHL (Inner Helmholtz layer), OHL (Outer Helmholtz layer) and GCL (Gouy-Chapman layer) [24].

The main physical processes occur in the conductive channel. Therefore, for further calculations, it is necessary to determine the surface potential of the interface between the semiconductor layer (channel) and insulator ϕ_{ch}. This can be calculated using Equation (1) and Equation (2) and expressions for the density of minority carriers in semiconductor. For ϕ_{ch} we receive:

$$\phi_{ch} = \varphi_T \ln\left(\frac{\eta C_{ox}\varphi_T N_A}{qtn_i^2}\right) + \varphi_T \ln\left\{\ln\left[1+\frac{1}{2}\exp\left(\frac{V_g - V_{th}}{\eta\varphi_T}\right)\right]\right\}. \tag{3}$$

where

$$\eta = 1+\frac{C_d}{C_{ox}} \approx 1+\sqrt{\frac{q\varepsilon_0\varepsilon_{Si}N_A}{2\varphi_T C_{ox}^2}}$$

is the factor of the transistor non-ideality (C_d is the capacitance of the silicon depletion layer per unit area).

We consider the case of an inversion *n*-channel liquid-gated FET (**Figure 1(c)**). It is clear that the majority of processes in the structure are therefore determined by the electrons. The channel source-drain current consists of drift and diffusion components. It is well known that the diffusion component is dominant in the sub-threshold mode and the drift component is dominant in the over-threshold region. The channel source-drain current in Y direction $I_{sd}(y)$ can be calculated using the following equation [8]:

$$I_{sd}(y) = \mu_{ef} w\left[Q_{ch}\frac{\mathrm{d}V_{sd}}{\mathrm{d}y} + \varphi_T\frac{\mathrm{d}Q_{ch}(y)}{\mathrm{d}y}\right]. \tag{4}$$

Here w is the channel width in Z direction, μ_{ef} is the effective mobility and Q_{ch} is the charge density of the channel mobile carriers ($[Q_{ch}] = [\mathrm{C/cm^2}]$):

$$Q_{ch} = \int_0^t qn\left(x, V_g\right)\mathrm{d}x. \tag{5}$$

Here t is the thickness of current channel in X direction, $n\left(x, V_g\right)$ is the electron's concentration in the channel. The behavior of the source-drain current is defined by the distribution of the concentration of the mobile charge carriers over the conducting channel. Obviously, the concentration of mobile carriers in the channel depends on both the coordinate x (see **Figure 1(a)**) and the applied gate voltage. At the same time, the charge surface concentration only depends on the gate voltage. Hence the overall concentration can be presented as follows:

$$n\left(x, V_g\right) = n_s\left(V_g\right) \times f\left(x, V_g\right). \tag{6}$$

Here $n_s\left(V_g\right)$ is the electron surface concentration per unit area at the oxide interface and $f\left(x, V_g\right)$ in unit of [$\mathrm{cm^{-1}}$] is the function which describes the charge carrier distribution in the X-Z plane of the channel (**Figure 1**) [25].

The surface concentration can be described using the unified charge control model from expression [26]:

$$V_g - V_{th} = \frac{q}{C_{ox}}\left(n_s - n_{s,t}\right) + \eta V_{th} \ln\left(\frac{n_s}{n_{s,t}}\right), \tag{7}$$

where $n_{s,t}$ is the surface density of electrons per unit area at the threshold voltage: $n_{s,t} = n_s$ at the $V_g = V_{th}$. It should be noted that the influence of the charge states of the electrolyte is determined by the value of V_{th} (see Equation (2)). The concentration $n_{s,t}$ can be expressed as:

$$n_{s,t} = \frac{\eta C_{ox} \varphi_T}{2q}. \tag{8}$$

Equation (7) has no analytical solution for n_s in terms of V_g. The following approximate solution is suitable for strong inversion and sub-threshold regimes [22]:

$$n_s = 2n_{s,t} \ln\left[1 + \frac{1}{2}\exp\left(\frac{V_g - V_{th}}{\eta \varphi_T}\right)\right]. \tag{9}$$

After determining $n_s\left(V_g\right)$, we must also calculate the function $f\left(x, V_g\right)$ in order to evaluate the influence of peculiarities of the carrier distribution on the physical processes taking place in the channel.

In order to find function $f\left(x, V_g\right)$ for the case of the quasi classical approach, we use the following dependence of $n(x)$ [8]:

$$n(x) = N_c \exp\left[-\frac{\left(E_c - q\phi(x)\right) - E_F}{k_B T}\right] = n_0 \exp\left[\frac{\phi(x)}{\varphi_T}\right]. \tag{10}$$

Here N_c is the density of states in the conduction band of a semiconductor, E_c is the semiconductor conduction band energy, $\phi(x)$ is the contact potential at the oxide-channel interface. To determine $\phi(x)$ we have to solve the Poisson equation:

$$\frac{\mathrm{d}^2\phi(x)}{\mathrm{d}x^2} = -\frac{\rho(x)}{\varepsilon_0 \varepsilon_{Si}}. \tag{11}$$

Here $\rho(x)$ is the space charge density for the fully ionized acceptor centers in semiconductor (usually it is boron in silicon):

$$\rho(x) = -q\left(N_A^- + n - p\right) = -qp_0\left[1 - \exp\left(-\frac{\phi}{\varphi_T}\right) + \frac{n_0}{p_0}\exp\left(\frac{\phi}{\varphi_T}\right)\right]. \tag{12}$$

Here n, p and n_0, p_0 are the concentrations of the non-equilibrium and equilibrium electrons and holes, respectively, N_A^- is the concentration of negatively charged acceptors. We can use following boundary conditions to solve Equation (11) (see **Figure 1**):

$$x \to \infty \Rightarrow \phi \to 0, \quad x \to 0 \Rightarrow \phi \to \phi_{ch}. \tag{13}$$

Using Equation (12) and boundary conditions (13), we obtain the following solution of Equation (11):

$$\phi(x)=\left\{\phi_{ch}+\frac{qn_0}{\varepsilon_0\varepsilon_{Si}}\left[1-\exp\left(-\frac{x}{l_s}\right)\right]\right\}\exp\left(-\frac{x}{l_s}\right), \tag{14}$$

where

$$l_s=\frac{L_D}{1+n_0/p_0},\quad L_D=\sqrt{\frac{\varepsilon_0\varepsilon_{Si}\varphi_T}{qp_0}}, \tag{15}$$

L_D is the Debye screening length.

Then using expression for ϕ_{ch} from Equation (3) finally we have for the function $f(x,V_g)$:

$$f(x,V_g)=\frac{n_0}{n_s}\times\exp\left\{\left[\ln\left(\frac{\eta\varphi_T C_{ox}N_A}{qtn_i^2}\right)+\ln\left[\ln\left(1+\frac{1}{2}\exp\left(\frac{V_g-V_{th}}{\eta\varphi_T}\right)\right)\right]\right.\right.$$
$$\left.\left.+\frac{qt^2n_i^2}{\varepsilon_0\varepsilon_{Si}\varphi_T N_A}\right]\exp\left(-\frac{x}{l_s}\right)\right\}. \tag{16}$$

The field caused by the applied gate voltage in the inversion layer of liquid-gated FETs changes the transport behavior of the charge carriers and results in more frequent scattering events than in the absence of the gate voltage. The carrier's mobility degrades as the result of scattering processes [27] [28] [29]. The mobility dependence on the transversal electric field (Y direction) at the applied gate voltage was taken into account using the following empiric equation [30]:

$$(\mu_{ef})_x=\mu_0-\theta(V_g+V_{th}), \tag{17}$$

where μ_0 is the low-field magnitude of the mobility, θ is the coefficient taken as 28 cm^2/(V^{2}s) [30] [31]. Since the modeling and the measurements are performed for low drain biases in linear mode, the effect of the electron velocity saturation on the drain current can be neglected. Other authors in [32] assume that when Coulomb scattering dominates the mobility dependence on the gate voltage $\mu(V_g)$ in the vicinity $V_g=V_{th}$ can be linearized in the form [33] [34]

$$\mu(V_g)=\mu_0+\theta(V_g-V_{th}), \tag{18}$$

where $\mu_0=\mu|_{V_g=V_{th}}$, $\theta=\left.\frac{\mathrm{d}\mu(V_g)}{\mathrm{d}V_g}\right|_{V_g=V_{th}}$, and in general case θ can be positive or negative.

In further calculations we will use expression (17) for the mobility of major carriers in the channel.

3. Source-Drain Current

Using Equation (4) and Equation (17) we can present the drift component of the source-drain current by following expression:

$$I_{sd}(y)\approx\frac{qwn_sV_{ds}}{l}\left[\mu_0-\theta(V_G+V_{th})\right]\int_0^t f(x,V_g)\mathrm{d}x,$$

where n_s is determined from Equation (9).

For the integral

$$\int_0^t f\left(x,V_g\right)\mathrm{d}x$$

we have

$$\int_0^t f\left(x,V_g\right)\mathrm{d}x=\frac{n_0}{n_s}\int_0^t \exp\left[G\exp\left(-\frac{x}{l_s}\right)\right]\mathrm{d}x\approx\frac{n_0}{n_s}t\left[1+\frac{l_s}{t}G\left(1-\mathrm{e}^{-t/l_s}\right)\right]. \quad (19)$$

Here

$$G\equiv\frac{1}{B}+\ln B+\ln\left[\ln\left(1+\frac{1}{2}\exp\left(\frac{V_g-V_{th}}{\varphi_T}\right)\right)\right],\quad B\equiv\frac{\varphi_T\varepsilon_0\varepsilon_{ox}N_A}{qt^2n_i^2}. \quad (20)$$

Thus

$$I_{sd}\left(y\right)\approx qwn_0V_{ds}\frac{t}{l}\left[\mu_0-\theta\left(V_G+V_{th}\right)\right]\left[1+\frac{l_s}{t}G\left(1-\mathrm{e}^{-t/l_s}\right)\right]. \quad (21)$$

Behavior of dependency I_{sd} from number of DNA molecules in solution N_{DNA} can be determined from dependency $V_{th}\left(Q_{ox}\right)$.

For simplicity of further calculations assume that $\eta\approx1$ and taking account that oxide layer capacitance for unit area

$$C_{ox}=\frac{\varepsilon_0\varepsilon_{ox}}{t}. \quad (22)$$

For V_{th} from (2) we have:

$$V_{th}=2\varphi_F+\phi_{dl}-\frac{\Phi_{Si}-\Phi_{ox}}{q}+\frac{Q_{ox}}{C_{ox}}. \quad (23)$$

Substituting (23) into (21) gives:

$$I_{sd}\left(Q_{ox}\right)\approx qwn_0V_{ds}\frac{t}{l}\left[\mu_0-\theta\left(V_G+2\varphi_F+\phi_{dl}-\frac{\Phi_{Si}-\Phi_{ox}}{q}+\frac{Q_{ox}}{C_{ox}}\right)\right]$$
$$\times\left\{1+\frac{l_s}{t}\left\{\frac{1}{B}+\ln B+\ln\left[\ln\left(1+\frac{1}{2}\exp\left(\frac{V_g+2\varphi_F+\phi_{dl}-\frac{\Phi_{Si}-\Phi_{ox}}{q}+\frac{Q_{ox}}{C_{ox}}}{\varphi_T}\right)\right)\right]\right\}\left(1-\mathrm{e}^{-t/l_s}\right)\right\}. \quad (24)$$

The influence of the oxide interface on the source-drain current of the transistor can be taken into account by the change of the charge of the oxide interface traps $Q_{ox}=qN_t$ (N_t is the surface concentration of oxide interface all proton donors and proton acceptors traps in units cm^{-2}, Figure 2). Depending on presence of negatively charged DNA molecules the charge on the oxide surface will decrease (compensated) and become

$$Q'_{ox}=qN_t^+\left(1-\delta\right),\quad \delta\equiv\frac{N_{\mathrm{DNA}}}{N_t^+}, \quad (25)$$

where N_t^+ and N_{DNA} are the surface concentrations of positively charged proton acceptor OH_2^+ traps (Figure 2) and DNA surface concentration in solution

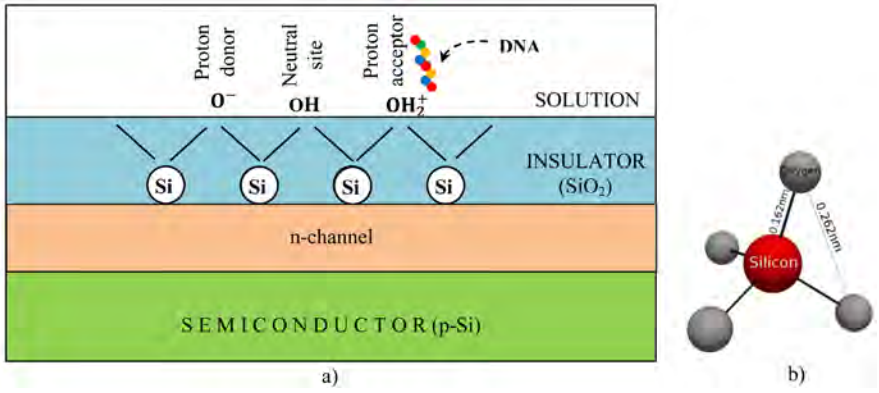

Figure 2. Site binding on the interface SiO_2-solution and the process of binding of the negatively charged DNA on the OH_2^+ free bond (a), SiO_2 tetrahedron structure (b).

near the oxide at a distance of the Debye length. It is clear that (25) is correct for the $N_{\text{DNA}} \le N_t^+$, or $\delta \le 1$. In the case of super compensation when $N_{\text{DNA}} > N_t^+$ the DNA additional molecules do not bind on the surface positively charged sites (proton acceptors, **Figure 2**) and ISFET biosenor do not sense this DNA additional molecules.

Figure 2 show site binding on the interface SiO_2-solution, process of negatively charged DNA molecule binding and silicon dioxide tetrahedron structure.

Consider the source-drain current sensitivity of the ISFET biosensor to DNA molecules S as a change in source-drain current ΔI_{sd} for a corresponding change in the proportion of DNA molecules in the solution $\Delta\delta$:

$$S = \left|\frac{\Delta I_{sd}}{\Delta\delta}\right|, \text{A} \tag{26}$$

As $\Delta\delta$ is dimensionless parameter sensitivity will be measured by the Ampere.

4. Numerical Simulation and Discussion

For numerical computation, we use the following values, which correspond to the sample geometry and the parameters of the materials for the investigated nanosize structure at the room temperature: $\mu_0 = 260\ \text{cm}^2/(\text{V}\cdot\text{s})$ [35], $\theta = 28\ \text{cm}^2/(\text{V}^2\cdot\text{s})$ [30] [31], $\varphi_T = 0.026\ \text{V}$, $N_{sol} = 0.015\ \text{mol/l}$ [25], $K_{AK}^+ = 0.001\ \text{mol/l}$ [25], $w = 150\ \text{nm}$, $l = 200\ \text{nm}$, $t = 20\ \text{nm}$, $\varepsilon_{Si} = 11.6$, $\varepsilon_{ox} = 3.9$, $\varepsilon_w \approx 80$, $\varepsilon_r \approx 78$, $\varepsilon_0 = 8.85\times10^{-14}\ \text{F/cm}$, $q = 1.6\times10^{-19}\ \text{C}$, $\Phi_{Si} = 4.85\ \text{eV}$ [36], $\Phi_{ox} = 5\ \text{eV}$ [36], $N_A = 10^{15}\ \text{cm}^{-3}$, $N_V = 2.5\times10^{19}\ \text{cm}^{-3}$ ($m_n^* = m_p^* \equiv m_0 = 9.1\times10^{-31}\ \text{kg}$, m_n^* and m_p^* are effective mass of electrons and holes, m_0 is the free electron mass), $p_0 \approx N_A = 10^{15}\ \text{cm}^{-3}$. Let's consider the case when "power of hydrogen" of the solution is equal to 7 ($\text{pH} = 7$). As

$$\text{pH} = -\log\left[\text{H}^+\right],$$

we get

$$\left[\text{H}^+\right] = 10^{-\text{pH}} = 10^{-7}\ \text{mol/l}.$$

For the electron concentration in the inversion layer we can assume that it is

equal to majority carrier's concentration in p-Si, e.g. $n_0(\text{inv}) \approx p_0 = 10^{15}\,\text{cm}^{-3}$. For the N_t^+ we can do following estimation. It is assumed that traps concentration on the interface silicon oxide-electrolyte is the same as silicon oxide-Si. According to data [36] traps concentration in Si-SiO_2 interface is about $\left(10^{10} - 10^{11}\right)\text{cm}^{-2}$. In further calculation we will use $N_t^+ \approx 10^{11}\,\text{cm}^{-2}$.

For numerical simulation let's simplify expression for source-drain current assuming that:

1) At the noted above parameters $B \propto 10^{10}$ and we can ignore term $\frac{1}{B}$ compared $\ln B$ as $\frac{1}{B} \ll \ln B$;

2) $$\left[\ln\left(1+\frac{1}{2}\exp\left(\frac{V_g + 2\varphi_F + \phi_{dl} - \frac{\Phi_{Si} - \Phi_{ox}}{q} + \frac{Q_{ox}}{C_{ox}}}{\varphi_T}\right)\right)\right] \approx \frac{1}{2}\exp\left(\frac{V_g + 2\varphi_F + \phi_{dl} - \frac{\Phi_{Si} - \Phi_{ox}}{q} + \frac{Q_{ox}}{C_{ox}}}{\varphi_T}\right);$$

3) $$\ln\left[\ln\left(1+\frac{1}{2}\exp\left(\frac{V_g + 2\varphi_F + \phi_{dl} - \frac{\Phi_{Si} - \Phi_{ox}}{q} + \frac{Q_{ox}}{C_{ox}}}{\varphi_T}\right)\right)\right] \approx \ln\frac{1}{2}\exp\left(\frac{V_g + 2\varphi_F + \phi_{dl} - \frac{\Phi_{Si} - \Phi_{ox}}{q} + \frac{Q_{ox}}{C_{ox}}}{\varphi_T}\right);$$

4) $1 - \text{e}^{-t/l_s} \approx 1 - \frac{t}{l_s}$.

Thus source-drain current can be presented as follows:

$$I_{sd} \approx \frac{qtwn_0V_{ds}}{l\varphi_T}\left[\mu_0 - \theta\left(V_G + 2\varphi_F + \phi_{dl} - \frac{\Phi_{Si} - \Phi_{ox}}{q} + \frac{Q_{ox}}{C_{ox}}\right)\right] \times\left[\varphi_T\left(1+\ln\frac{B}{2}\right) + V_g + 2\varphi_F + \phi_{dl} - \frac{\Phi_{Si} - \Phi_{ox}}{q} + \frac{Q_{ox}}{C_{ox}}\right]. \quad (27)$$

Results of numerical calculations of source-drain current I_{sd} vs source-drain voltage V_{ds} and DNA concentration are presented in **Figures 3-5**. The error in plotting the dependencies in **Figures 3-5** does not exceed (5 - 7)%. In order not to complicate the graphs, these errors are not shown in the figures. Note that fluctuations of values by (5 - 7)% particularly do not affect the course of dependencies and do not change the mechanisms for explaining their behavior. As expected, the dependence of I_{sd} on the source-drain voltage is linear. Dependency I_{sd} vs DNA concentration N_{DNA} (or δ) is very weak (see **Figure 4**). At the beginning ($0 < \delta < 0.1$) source-drain current increases very weakly. This

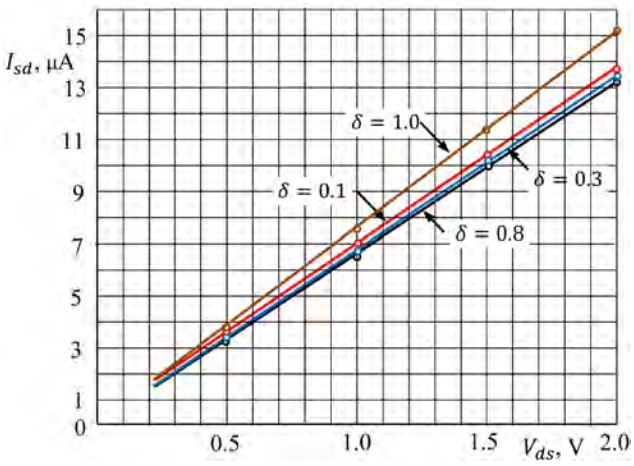

Figure 3. Dependency of the source-drain current vs source-drain voltage.

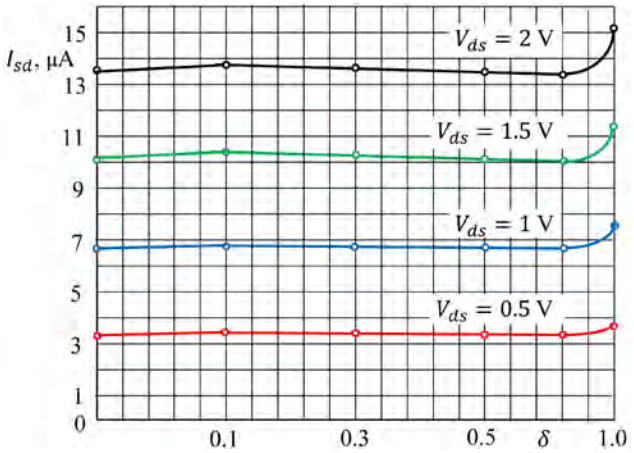

Figure 4. Dependency of the source-drain current vs DNA molecules concentration in solution.

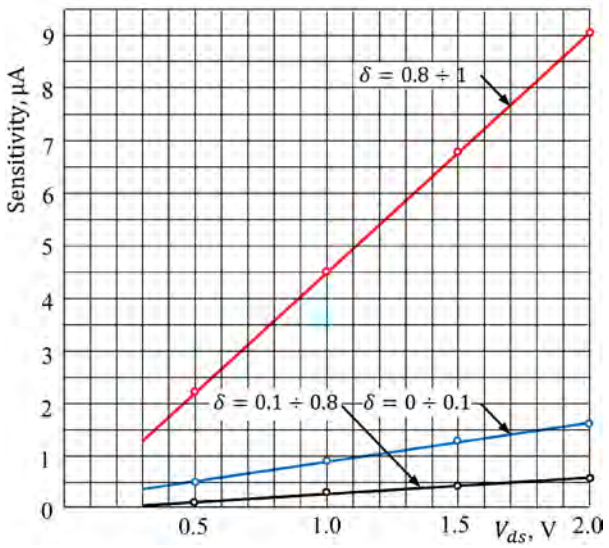

Figure 5. Dependency of the current sensitivity vs. source-drain voltage at the several values of DNA molecules concentration N_{DNA} or δ.

behavior can be explained as follows. Assume that all proton donors (OH^-) sites in the interface oxide-electrolyte (**Figure 2**) fully accept protons (H^+) from solution and changes in their charges are not significant and can be neglected during the sensor operation. At low concentration of DNA molecules $0 < \delta < 0.1$, they are bind very weakly or not bind with free proton acceptor sites OH_2^+ due to its high diffusion activity and the presence of a Coulomb barrier near proton acceptor sites. With increasing DNA concentration and therefore decreasing their diffusion activity (when $0.1 < \delta < 0.8$) negatively charged DNA molecules overcome Coulomb barrier near the proton acceptor sites and bond with them on the oxide surface. As a result the positive surface charge decreases and correspondingly decreases deepness of current channel and its conductivity (source-drain current). At the super compensation of the proton acceptor sites OH_2^+ ($\delta \to 1$, high concentration of DNA molecules) in oxide-electrolyte interface $I_{sd}(\delta)$ dependency has increasing behavior. Probably it is conditioned by the ionic Coulomb blockade effect [37]. As it is known this effect appears in the electro-diffusive transport of charged ions (in our case DNA molecules) through sub-nanometer artificial nanopores [38] or biological ion channels [39]. DNA molecules cannot overcome Coulomb barrier of the proton acceptor sites and channel conductance again increase. Consequently, the current increases.

The dependence of current sensitivity on source-drain voltage for several values of DNA molecules concentration is presented in **Figure 5**. These dependencies are constructed according to formula (26) using the data in **Figure 4**. They are also linear dependency. Depending on values of DNA concentration in solution and source-drain applied voltage current sensitivity can reach comparatively high values (up to 5 … 9 μA/δ in the case of parameters chosen above).

Based on the above reasoning, we can draw the following conclusions.

- ✓ ISFET nanosized structures can be used for detecting charged DNA molecules.
- ✓ The influence of DNA molecules on the work of ISFET biosensors is manifested by a change in the magnitude of the surface charge of the gate electrode.
- ✓ Starting with fairly low concentrations of DNA, ISFET biosensors respond to the presence of DNA molecules in an aqueous solution which is manifested by modulation of channel conductance or the source-drain current.
- ✓ Current sensitivity linearly depends on the source-drain voltage and reaches high values.

Thus, ISFET nanosized silicon biosensors can be successfully used to detect very low concentrations of DNA molecules in an aqueous solution with high sensitivity. As an advantage note also the compatibility of silicon based devices with modern CMOS technology.

Conflicts of Interest

The authors declare no conflicts of interest regarding the publication of this paper.

References

[1] Bergveld, P. (1970) Development of an Ion Sensitive Solid State Device for Neurophysiological Measurements. *IEEE Transactions on Biomedical Engineering*, **BME-17**, 70-71. https://doi.org/10.1109/TBME.1970.4502688

[2] Caras, S. and Janata, J. (1980) Field Effect Transistor Sensitive to Penicillin. *Analytical Chemistry*, **52**, 1935-1937. https://doi.org/10.1021/ac50062a035

[3] Lee, C.-S., Kim, S.K. and Kim, M. (2009) Ion-Sensitive Field-Effect Transistor for Biological Sensing. *Sensors*, **9**, 7111-7131. https://doi.org/10.3390/s90907111

[4] Veigas, B., Fortunato, E. and Baptista, P.V. (2015) Field Effect Sensors for Nucleic Acid Detection: Recent Advances and Future Perspectives. *Sensors*, **15**, 10380-10398. https://doi.org/10.3390/s150510380

[5] Hu, Y. (2015) Advanced Sensing and Processing Methodologies for ISFET Based DNA Sequencing. Imperial College London, London.

[6] Ingebrandt, S., Han, Y., Nakamura, A., Poghossian, A., Schöning, M.J. and Offenhausser, A. (2007) Label-Free Detection of Single Nucleotide Polymorphisms Utilizing the Differential Transfer Function of Field-Effect Transistors. *Biosensors and Bioelectronics*, **22**, 2834-2840. https://doi.org/10.1016/j.bios.2006.11.019

[7] Goncalves, D., Prazeres, D., Chu, V. and Conde, J. (2008) Detection of DNA and Proteins Using Amorphous Silicon Ion-Sensitive Thin-Film Field Effect Transistors. *Biosensors and Bioelectronics*, **24**, 545-551.

[8] Sze, S.M. (1986) Physics of Semiconductor Devices. Wiley, New York.

[9] Veigas, B., Branquinho, R., Pinto, J.V., Wojcik, P.J., Martins, R., Fortunato, E. and Baptista, P.V. (2014) Ion Sensing (EIS) Real-Time Quantitative Monitorization of Isothermal DNA Amplification. *Biosensors and Bioelectronics*, **52**, 50-55. https://doi.org/10.1016/j.bios.2013.08.029

[10] Wong, M.L. and Medrano, J.F. (2005) Real-Time PCR for mRNA Quantitation. *BioTechniques*, **39**, 75-85. https://doi.org/10.2144/05391RV01

[11] Branquinho, R., Veigas, B., Pinto, J.V., Martins, R., Fortunato, E. and Baptista, P.V. (2011) Real-Time Monitoring of PCR Amplification of Proto-Oncogene c-MYC Using a Ta_2O_5 Electrolyte-Insulator-Semiconductor Sensor. *Biosensors and Bioelectronics*, **28**, 44-49. https://doi.org/10.1016/j.bios.2011.06.039

[12] Toumazou, C., Shepherd, L., Reed, S., Chen, G., *et al.* (2013) Simultaneous DNA Amplification and Detection Using a pH-Sensing Semiconductor System. *Nature Methods*, **10**, 641-646.

[13] Kaisti, M., Kerko, A., Aarikka, E., Saviranta, P., Boeva, Z., Soukka, T. and Lehmusvuori, A. (2017) Real-Time Wash-Free Detection of Unlabeled PNA-DNA Hybridization. *Scientific Reports*, **7**, Article No. 15734. https://doi.org/10.1038/s41598-017-16028-7

[14] Purushothaman, S., Toumazou, C. and Ou, C. (2006) Protons and Single Nucleotide Polymorphism Detection: A Simple Use for the Ion Sensitive Field Effect Transistor. *Sensors and Actuators B*: *Chemical*, **114**, 964-968. https://doi.org/10.1016/j.snb.2005.06.069

[15] Gasparyan, F., Zadorozhnyi, I., Khondkaryan, H., Arakelyan, A. and Vitusevich, S. (2018) Photoconductivity, pH Sensitivity, Noise, and Channel Length Effects in Si Nanowire FET Sensors. *Nanoscale Research Letters*, **13**, 87-96. https://doi.org/10.1186/s11671-018-2494-5

[16] Gasparyan, F., Zadorozhnyi, I., Khondkaryan, H., Arakelyan, A. and Vitusevich, S. (2017) Biochemical Sensors Based on Silicon Nanoribbon FETs. Part 1: Samples

Fabrication, CVCs, pH-Sensitivity. *Proceedings of* 11*th International Conference on Semiconductor Micro- & Nanoelectronics*, Yerevan, Armenia, 23-25 June 2017.

[17] Gasparyan, F.V. and Khondkaryan, H.D. (2015) Low-Frequency Noises and SNR of Double Gated Si NW ISFET Based Biochemical Sensor. *Proceedings of* 10*th International Conference on Semiconductor Micro- & Nanoelectronics*, Yerevan, Armenia, 11-13 September 2015, 68-71.

[18] Gasparyan, F.V., Poghossian, A., Vitusevich, S.A., Petrychuk, M.V., Sydoruk, V.A., Siqueira, J.R., Oliveira, O.N., Offenhäusser, A. and Schöning, M.J. (2011) Low-Frequency Noise in Field-Effect Devices Functionalized with Dendrimer/Carbon-Nanotube Multilayers. *IEEE Sensors Journal*, **11**, 142-149. https://doi.org/10.1109/JSEN.2010.2052355

[19] Deen, M.J., Shinwari, M.W., Ranuárez, J.C. and Landheer, D. (2006) Noise Considerations in Field-Effect Biosensors. *Journal of Applied Physics*, **100**, Article ID: 074703. https://doi.org/10.1063/1.2355542

[20] Hassibi, A., Navid, R., Dutton, R.W. and Lee, T.H. (2004) Comprehensive Study of Noise Processes in Electrode Electrolyte Interfaces. *Journal of Applied Physics*, **96**, 1074-1082. https://doi.org/10.1063/1.1755429

[21] Janicki, M., Daniel, M., Szermer, M. and Napieralski, A. (2004) Ion Sensitive Field Effect Transistor Modelling for Multidomain Simulation Purposes. *Microelectronics Journal*, **35**, 831-840. https://doi.org/10.1016/j.mejo.2004.06.015

[22] Ytterdal, T., Cheng, Y. and Fjeldly, T.A. (2003) Device Modeling for Analog and RF CMOS Circuit Design. John Wiley & Sons, New York. https://doi.org/10.1002/0470863803

[23] Tarasov, A., Wipf, M., Stoop, R.L., Bedner, K., Fu, W., Guzenko, V.A., Knopfmacher, O., Calame, M. and Scho, C. (2012) Understanding the Electrolyte Background for Biochemical Sensing with Ion-Sensitive Field-Effect Transistors. *ACS Nano*, **6**, 9291-9298. https://doi.org/10.1021/nn303795r

[24] Nakamura, M., Sato, N., Hoshi, N. and Sakata, O. (2011) Outer Helmholtz Plane of the Electrical Double Layer Formed at the Solid Electrode-Liquid Interface. *ChemPhysChem*, **12**, 1430-1434. https://doi.org/10.1002/cphc.201100011

[25] Pud, S., Gasparyan, F., Petrychuk, M., Li, J., Offenhausser, A. and Vitusevich, S.A. (2014) Single Trap Dynamics in Electrolyte-Gated Si-Nanowire Field Effect Transistors. *Journal of Applied Physics*, **115**, Article ID: 233705. https://doi.org/10.1063/1.4883757

[26] Gao, X.P.A., Zheng, G. and Lieber, C.M. (2010) Subthreshold Regime has the Optimal Sensitivity for Nanowire FET Biosensors. *Nano Letters*, **10**, 547-552. https://doi.org/10.1021/nl9034219

[27] Sabnis, A.G. and Clemens, J.T. (1979) Characterization of the Electron Mobility in the Inverted (100) Si Surface. *International Electron Devices Meeting*, **25**, 18-21. https://doi.org/10.1109/IEDM.1979.189528

[28] Woo, J. and Cheng, B. (1996) Measurement and Modeling of the N-Channel and P-Channel MOSFET's Inversion Layer Mobility at Room and Low Temperature Operation. *Journal de Physique IV Colloque*, **6**, C3-43-C3-47.

[29] Zhou, X. and Lim, K.Y. (2000) A Novel Approach to Compact I-V Modeling for Deep-Submicron MOSFET's Technology Development with Process Correlation. *Technical Proceedings of the International Conference on Modeling and Simulation of Microsystems* (*MSM* 2000), San Diego, CA, 27-29 March 2000, 333-336.

[30] Park, C., Lee, C., Lee, K., Moon, B.-J., Byun, Y.H. and Shur, M. (1991) A Unified Current-Voltage Model for Long-Channel nMOSFETs. *IEEE Transactions on Elec-*

tron Devices, **38**, 399-406. https://doi.org/10.1109/16.69923
https://www.academia.edu/23535536/A_unified_current-voltage_model_for_long-channel_nMOSFETs

[31] Gildenblat, G.S. and Huang, C.-L. (1989) Engineering Model of Inversion Channel Mobility for 60-300k Temperature Range. *Electronics Letters*, **25**, 634-636. https://doi.org/10.1049/el:19890430

[32] Rudenko, T., Kylchitska, V., Khairuddin, M. Arshad, M., Raskin, J.-P., Nazarov, A. and Flandre, D. (2011) On the MOSFET Threshold Voltage Extraction by Transconductance and Transconductance-to-Current Ratio Change Methods: Part I—Effect of Gate-Voltage-Dependent Mobility. *IEEE Transactions on Electron Devices*, **58**, 4172-4178. https://doi.org/10.1109/TED.2011.2168226

[33] Takagi, S., Iwase, M. and Toriumi, A. (1988) On the Universality of Inversion-Layer Mobility in N- and P-Channel MOSFETs. *Technical Digest*, *International Electron Devices Meeting*, San Francisco, CA, 11-14 December 1988, 398-401. https://doi.org/10.1109/IEDM.1988.32840

[34] Tsuno, M., Suga, M., Tanaka, M., Shibahara, K., Miura-Mattausch, M. and Hirose, M. (1999) Physically-Based Threshold Voltage Determination for MOSFETs of All Gate Lengths. *IEEE Transactions on Electron Devices*, **46**, 1429-1434. https://doi.org/10.1109/16.772487

[35] Jeong, C., Antoniadis, D. and Lundstrom, M.S. (2009) On Backscattering and Mobility in Nanoscale Silicon MOSFETs. *IEEE Transactions on Electron Devices*, **56**, 2762-2769. https://doi.org/10.1109/TED.2009.2030844

[36] Pantelides, S.T., Wang, S., Franceschetti, A., *et al.* (2006) Si/SiO_2 and SiC/SiO_2 Interfaces for MOSFETs-Challenges and Advances. *Materials Science Forum*, **527-529**, 935-948. https://doi.org/10.4028/www.scientific.net/MSF.527-529.935

[37] Krems, M. and Di Ventra, M. (2013) Ionic Coulomb Blockade in Nanopores. *Journal of Physics*: *Condensed Matter*, **25**, Article ID: 065101. https://doi.org/10.1088/0953-8984/25/6/065101

[38] Feng, J., Liu, K., Graf, M., Dumcenco, D., Kis, A., Di Ventra, M. and Radenovich, A. (2016) Observation of Ionic Coulomb Blockade in Nanopores. *Nature Materials*, **15**, 850-855. https://doi.org/10.1038/nmat4607

[39] Kaufman, I.K., McClintock, P.V.E. and Eisenberg, R.S. (2015) Coulomb Blockade Model for Permeation and Selectivity in Biological Ion Channels. *New Journal of Physics*, **17**, Article ID: 083021. https://doi.org/10.1088/1367-2630/17/8/083021

Scientific Research Publishing

Open Journal of Biophysics, 2019, 9, 254-266
https://www.scirp.org/journal/ojbiphy
ISSN Online: 2164-5396
ISSN Print: 2164-5388

Seed Germination and Their Photon Emission Profile Following Exposure to a Rotating Magnetic Field

Victoria L. Hossack*, Michael A. Persinger, Blake T. Dotta*

Behavioural Neuroscience and Biology Programs, Laurentian University, Sudbury, Ontario, Canada
Email: *vx_hossack@laurentian.ca, *bx_dotta@laurentian.ca

How to cite this paper: Hossack, V.L., Persinger, M.A. and Dotta, B.T. (2019) Seed Germination and Their Photon Emission Profile Following Exposure to a Rotating Magnetic Field. *Open Journal of Biophysics*, **9**, 254-266.
https://doi.org/10.4236/ojbiphy.2019.94018

Received: July 26, 2019
Accepted: August 24, 2019
Published: August 27, 2019

Abstract

A multitude of experiments have applied magnetic fields to plants or seeds and found a variety of different and sometimes contradicting results. A magnetic field generating device called the Chrysalis resonator has been shown to influence the brain activity of human participants, the photon emissions from bacteria, mammalian cell cultures and water. In this experiment sunflower seeds (*Helianthus annus*) were allowed to begin germination and then exposed to either the field generated by the Chrysalis resonator or a sham condition. Their growth and photon emissions were taken over the next 5 days. It was found that the seeds showed less germination 48 hours after exposure and significantly higher photon emissions when 3 seeds were measured together in a dish, but not if 2 seeds or 1 seed were measured. There were no significant differences in the photon measurements from the water the seeds were germinating in. These results may indicate that the seeds became more sensitive to the presence of neighbouring seeds. The photon emissions results were also significantly impacted by external weather conditions.

Keywords

Seed Germination, Photon, Communication, Magnetic Field

1. Introduction

The characteristics of magnetic field treatments previously used to treat plants are highly variable, and so are the results [1] [2]. Some consistent findings seem to be reduced growth when high frequency (GHz) magnetic fields such as from cell phones or Gunn generators (produce fields in the microwave frequencies)

are used [3]. While the high frequency magnetic fields in [3] are man-made and produce decreases in plant growth, there have been other magnetic fields that have similar frequencies to powerlines and electrical outlets (50 - 60 Hz) that have shown positive [4] [5] and negative [6] effects in growth. A review of experiments that investigated the effects of reducing the background intensity of the geomagnetic field (either using a Faraday cage-like device or active shielding) also found there was a trend of reduced growth [7]. One study [8] decreased the intensity of the X-component of the geomagnetic field, and found that these conditions could either increase or decrease plant growth depending on the geomagnetic storms conditions.

Studies that apply low intensity magnetic fields with frequencies that converge on the Schumann frequency seem to increase plant growth measures [9] [10] [11] [12]. For example, one study [11] used a 1500 nT field (~20 times weaker than the geomagnetic field) at frequencies of 0.1 to 100 Hz to pretreat seeds, and found that exposure to a 10 Hz field was the most effective at increasing germination, water absorption, and electrical conductivity of the seed leachates. The changes in the electrical conductivity were associated with a more acidic pH and could indicate that the magnetic field-treated seeds had an altered ion exchange with their external environment [11]. Increased germination was found with exposure to a 400 - 500 μT field (~10 times stronger than the geomagnetic field) that was applied at frequencies of 1 to 1000 Hz, with 10 Hz having the largest increase in germination [9]. Recently, researchers applied a magnetic field of 300 μT (~10 times stronger than the geomagnetic field) at 7.83 Hz (the Schumann frequency) and found an increase in germination compared to controls [12]. Experiments utilizing static magnetic fields that are in the milliTesla intensity range show a high variability of results with findings of decreased [13] and increased growth [14] [15].

Biological organisms emit photons [16]-[23], including plants [14] [24]-[30]. One study that measured photon emissions from seeds, found that they could manipulate the number of photons by altering the temperature and humidity, factors involved in the onset of germination [30]. They also dissected the seeds and determined that the source of photon emissions was specifically from the inner layer of the seed coat surrounding the seed embryo, indicating that it may be involved in signaling the seed to begin germinating [30]. In addition to communication within the organism, photon emissions have also been demonstrated as a method of communication between organisms [17] [18] [23].

Our lab has been conducting research on a series of devices known as the resonator. These devices have been demonstrated to influence the growth of bacteria [31]. This experiment was designed to start testing this device on a different type of biological organism to see if there were any universal effects of this device or if its effects are specific to bacteria. Magnetic fields are increasing in popularity in everything from agriculture to disease treatment and therefore understanding the width of their effects is important.

2. Methods

2.1. Seed Germination Preparation

Sunflowers (*Helianthus annus*) were obtained from the gardening section of a local department store (subtype, Russian mammoth). For each trial, 108 seeds were split between two solutions of 25 mL of a 5% bleach solution, submerged for 5 minutes and then washed with tap water. The seeds were put into 100 mm petri dishes with 10 mL of President's Choice spring water for germination, with 18 seeds per dish. In each trial there were three 100 mm dishes in each condition. Three trials were completed of this experiment.

2.2. Rotating Magnetic Field Device

The magnetic field device used in this experiment is known as the Chrysalis resonator. It is one model of many that produces a magnetic field around 110 Hz. In this model the exact peak frequency of the magnetic field was 113 Hz. The magnetic field has a strength of approximately 0.75 Gauss, or 75 μT. A description of a similar model of this device has been previously published [31] and can also be found in the patent (Canadian Patent No. CA 2631215). Briefly, the magnetic field is generated by cylinders that rotate within the device at about 3000 - 4000 rotations per minute when the device is on. The cylinders inside the device are arranged in a circle and contain puck magnets, these rotating puck magnets are responsible for generating the magnetic field.

2.3. Procedure

After the seeds were placed into their dishes, they were placed directly on the Chrysalis resonator for 1 hour to either be exposed to the field or to the sham condition (field OFF but with the fan running). Both conditions were complete on the same day with an hour between exposures. When not being exposed and during germination, the seeds were placed on flat surfaces in the dark. Starting 24 hours after exposure, daily measurements were taken for five days to determine if each seed had begun to germinate and to measure the length of the root/stem that had emerged from the shell. Statistical analysis of the length measurements were complete only on the seeds that had begun germination.

After taking growth measurements, photon measurements were taken on a photomultiplier tube (PMT). The PMT was model DM0089C, which is most sensitive to photons of wavelengths between 280 to 630 nm. For preparation, 6 seeds were picked from each condition that were within a range of seedling length measurements that had been taken that day (**Table 1**). These were then put into three 35 mm dishes; in the first dish there was one seed, in the second dish there were two seeds and in the third dish there were three seeds. Each of these dishes contained 0.5 mL of fresh spring water, this was to reduce the amount of stress that may have been occurring by measuring these seeds. Additionally, there were 35 mm dishes measured that contained 1 mL of spring water from the dishes of germinating seeds.

Table 1. Approximate range of root/stem lengths of seeds that were chosen from each condition to be used for photon measurements.

Day of Measurement	Range of seedling length (in millimetres)
1	0 - 1
2	1 - 2
3	2 - 7
4	9 - 30
5	30 - 80

The PMT was housed in a black-painted wooden box that was covered in black towels. The seed dishes were placed on top of the PMT aperture. Samples were measured three times for one minute intervals at a sampling rate of 50 Hz. For statistical analysis, the average of the second and third recording was used. The first recording was not used to reduce the effect of light pollution. An example of a recording can be seen in Figure 1, from this the mean of all the points was computed as well as the standard deviation of all the points.

3. Results

3.1. Germination

Seeds were germinated in 100 mm petri dishes, with 18 seeds in one dish. The percent number of seeds in each dish that germinated were calculated for each day for both the magnetic field exposure and sham condition. The average was taken of the three dishes in each condition. There was a significant interaction between day of measure and the field condition [$F(4, 16) = 4.51$, $p = 0.013$; $p\eta^2 = 0.53$; Figure 2]. There was a significant decrease in the proportion of seeds which germinated for the magnetic field condition compared to the sham condition. Paired t-tests for each condition showed the interaction comes from difference in slope between day 1 and day 2 for the two conditions (Figure 2), evident in the disparity between the t-statistics (Table 2). This indicates that the effect on germination rate wasn't evident until the day 2 measurement, which was taken 48 hours after exposure.

Length of seedling was then measured for the seeds that had germinated. There was no significant difference between the field exposed of sham exposed seedlings [$F(4, 16) = 0.45$, $p = 0.770$; Figure 3].

3.2. Photon-Seed

Initial results indicated no significant effects, however there was a large variability between the average number of photons between the different replicate of experiments [$F(2, 17) = 15.2$, $p < 0.001$, $\Omega^2 = 19.3\%$; Figure 4], as well as large differences in the standard deviation of the number of photons [$F(2, 17) = 27.0$, $p < 0.001$, $\Omega^2 = 24.8\%$; Figure 4]. In both variables, Tukey's post hoc test determined that the second replicate was significantly higher than the first and third replicate ($p < 0.05$).

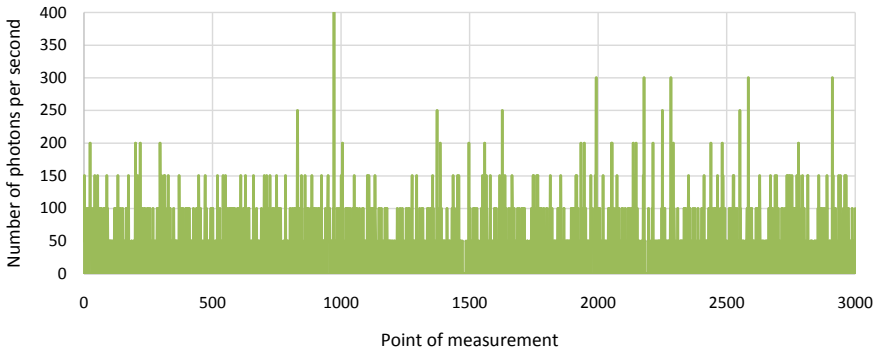

Figure 1. Example of 1 minute recording of seeds on photomultiplier tube. One measurement was taken every 20 milliseconds (sampling rate of 50 Hz).

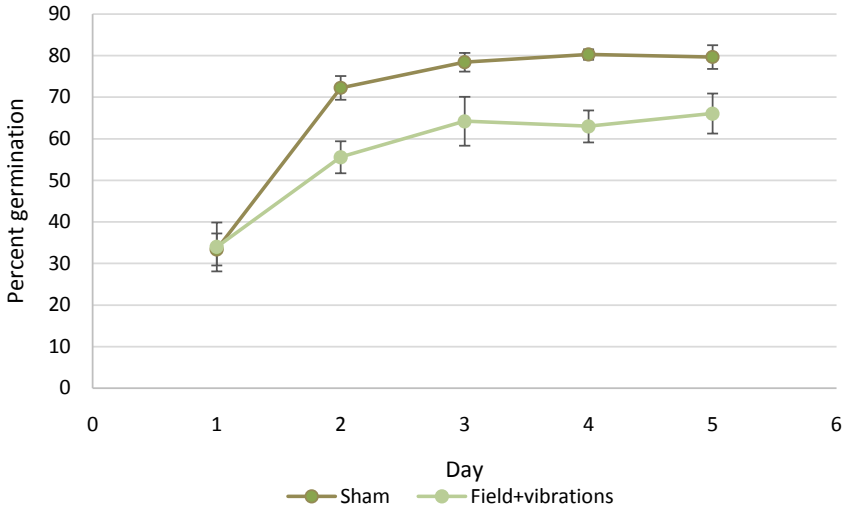

Figure 2. The percent number of seeds that germinated over 5 days in the dark, resting in spring water. Seeds begun germination at Day 0 and were subsequently exposed to one of the conditions. Error bars represent SEM.

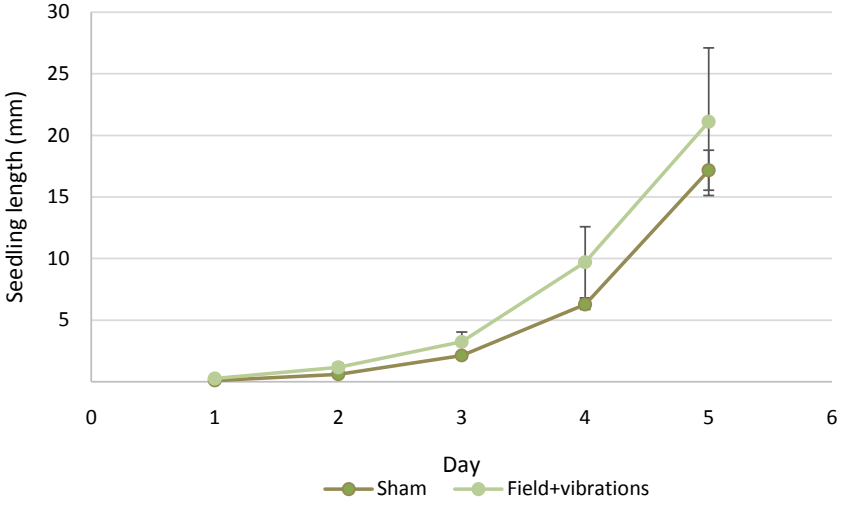

Figure 3. The length of seedling over the 5 days of germination in the dark. Seeds begun germination at Day 0 and were subsequently exposed to one of the conditions. Error bars represent SEM.

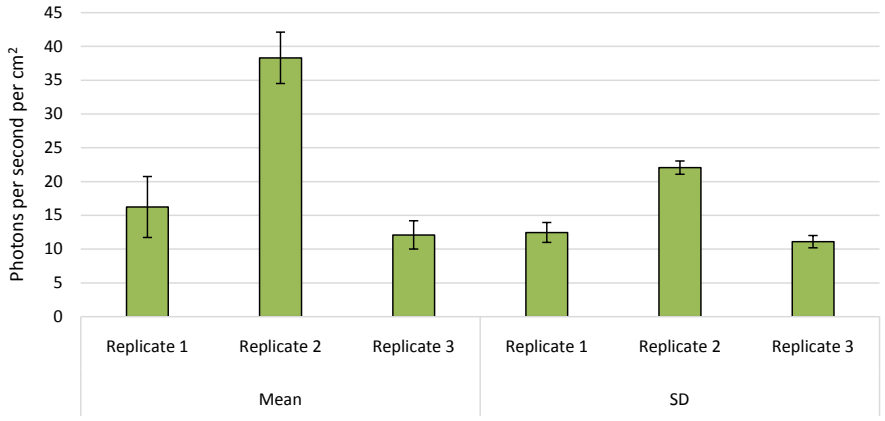

Figure 4. Difference across in mean and standard deviation (SD) photons in the three different replicates. Error bars represent the SEM.

Table 2. Paired t-tests between the 5 days of measurement for the different magnetic field conditions. Values represent the t-statistic which had 2 degrees of freedom.

	Day 1 to 2	Day 2 to 3	Day 3 to 4	Day 4 to 5
Sham	18.2*	1.25	1.73	0.378
Field	9.71*	2.14	0.555	2.50

* = $p < 0.05$.

Due to this large variability between replicates, two statistical methods were used for further analysis. The first was entering weather variables into the dataset, to see if controlling for any of these removed the variability. Second, within-subjects z-scores for each replicate were used as well to confirm any results found with the weather variables.

Weather variables included in the dataset were the daily and hourly average of temperature, relative humidity and AP index. Also included were the hour of day (in Eastern Standard Time) the measurements were taken and the day of year the replicate began. Using a series of multivariate analysis of covariances (MANCOVAs) it was determined that most of the significant covariates were from the between subjects analysis (between the three replications) and not the within subjects analyses (within each single replication) (**Table 3**). Temperature and humidity explained the most variance when using the values for the hour of photon measurement, whereas the AP index explained the most variance when using the daily average values (**Table 3**). A regression analysis was used with all of the weather variables and the mean number of photons. The only variable that entered as a predictor was the daily average AP index [$F(1, 17) = 32.4$, $p \leq 0.001$, $r^2 = 0.648$; **Table 4**].

The residuals from this analysis were saved as a new variable and analyzed in a two-way ANOVA, finding a significant main effect for the number of seeds [$F(2, 17) = 9.40$, $p = 0.003$] and a significant two way interaction between the number of seeds and resonator condition [$F(2, 17) = 4.28$, $p = 0.040$; **Figure 5(b)**]. Tukey's post-hoc test determined this was being driven by the 3 seeds group in the

Table 3. F-values from multivariate analysis of covariance with weather variables from the hour of photon measurement or the daily average. Included are the effect sizes, represented as partial eta^2 ($p\eta^2$).

		Mean photons per second per cm^2		SD photons per second per cm^2	
Covariate	Statistic	Between-subjects	Within-subjects	Between-subjects	Within-subjects
Temperature of hour	F- statistic	46.3**	0.84	80.7**	2.83
	$p\eta^2$	0.81	0.018	0.88	0.057
Temperature, daily average	F- statistic	0.20	0.00	0.12	1.33
	$p\eta^2$	0.018	0.0001	0.011	0.028
Humidity of hour	F- statistic	47.6**	1.87	83.7**	4.60*
	$p\eta^2$	0.81	0.038	0.88	0.089
Humidity, daily average	F- statistic	4.48	1.00	5.64*	0.02
	$p\eta^2$	0.29	0.021	0.34	0.0005
Ap index of hour	F- statistic	4.31	11.6*	4.11	10.8*
	$p\eta^2$	0.28	0.20	0.27	0.19
Ap index, daily average	F- statistic	79.7**	4.93*	168.4**	3.81
	$p\eta^2$	0.88	0.095	0.94	0.075
Hour of measurement	F- statistic	30.1**	3.23	35.2**	3.82
	$p\eta^2$	0.73	0.064	0.76	0.075
Day of year	F- statistic	0.66	Cannot compute	0.53	Cannot compute
	$p\eta^2$	0.057		0.046	

*p < 0.05; **p < 0.001.

Table 4. Regression statistics of the daily AP index predicting the mean photons per second per cm^2 in germinating seedlings.

Variable	Regression	r^2	B	Std Err of B	Beta
Daily AP	0.82	0.65	6.53	1.15	0.818
Constant			−20.5	7.77	

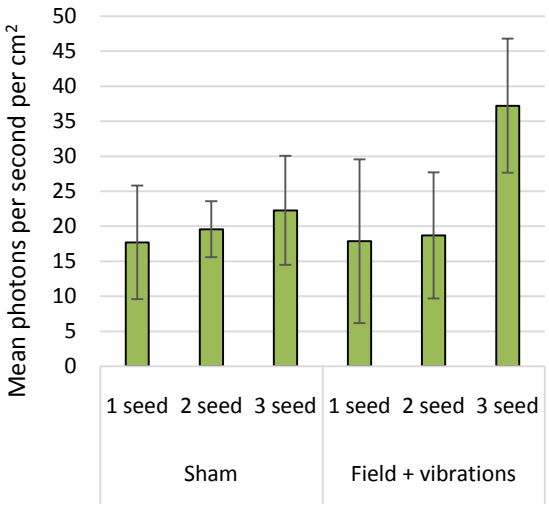

(a)

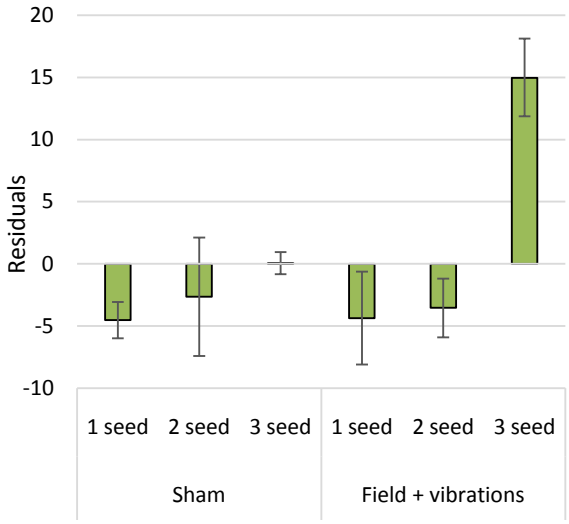

(b)

Figure 5. Mean photon emissions per second per cm^2 (assumed diameter of 2.5 cm for PMT aperture) across the different conditions in a resonator experiment. (a) Original values. (b) Residuals after counting for daily average AP index. Error bars represent SEM.

resonator condition being significantly higher than all other groups ($p < 0.05$). When an analysis was carried out on the SD of photons, the same main effect for number of seeds [$F(2, 17) = 7.47$, $p = 0.008$] and interaction [$F(2, 17) = 12.0$, $p = 0.001$] were found.

Another analysis was then carried out, using within subject z-scores, to see if this would show the same result found above. For this analysis the dataset had to be re-organized. The measurements were averaged over the 5 days into one value and the within-subject component became the number of seeds that were measured and the within-subject z-scores were computed. When a MANOVA was used on the mean number of photons, the effect for number of seeds was still present [$F(2, 8) = 5.58$, $p = 0.030$], where paired t-tests showed that the 3 seed group was significantly greater than the 1 seed group ($p < 0.05$); but the there was no longer an interaction with resonator condition [$F(2, 8) = 1.25$, $p = 0.336$]. When this same analysis was used with the standard deviation of photons, there was no longer a significant main effect of number of seeds [$F(2, 8) = 3.51$, $p = 0.080$] but the interaction between number of seeds and resonator condition was significant [$F(2, 8) = 4.67$, $p = 0.045$; **Figure 6**]. Paired t-tests showed that none of the groups were significantly different in the Sham condition ($p > 0.05$) but that in the Field + vibrations condition, the 3seed was group was significantly greater than the 2 seed and the 1 seed group ($p < 0.05$). These are the same differences found between groups as was found in the residual analysis for the standard deviation of photon recordings.

3.3. Photon-Water

There were no differences between the sham and field condition in the photon emissions measured from the water the seeds had been germinating in ($p >$

0.05). Similar to the seeds, the mean AP index for the day of measurement was a significant predictor of mean photons (Table 5). A similar relationship was found with the SD of photons recorded. When residuals were used in an ANOVA there was no significant effect between conditions for the mean [F(1, 5) = 0.481, p = 0.526] or SD of photons [F(1, 5) = 0.768, p = 0.430].

4. Discussion

Exposure to the dynamic field of the Chrysalis resonator (and its vibrations) caused approximately a 15% decrease in the number of seeds that germinated. This appeared in the measurements 48 hours after exposure, while there was no difference in germination 24 hours after exposure. Delayed effects of magnetic field exposure on germination have been previously reported [14] [15]. In a recent study involving seed germination and magnetic fields [15], authors found greatest differences between the magnetic field and sham groups at 96 hours after exposure. Decreased germination is an effect previously found with high frequency man-made fields [3] or environments that reduced the background intensity of the Earth's static magnetic field [7]. Is it possible that these two broad categories of magnetic field treatments are reducing a developing seeds coherence or connection with the Earth's magnetic field? The phenomenon of this type of coherence has already been demonstrated in humans [32] [33] [34], where

Table 5. Regression statistics of the daily AP index predicting the mean photons per second per cm^2 in spring water seeds were germinating in.

Variable	Regression	r^2	B	Std Err of B	Beta
Daily AP	0.97	0.94	0.802	0.094	0.974
Constant			−3.48	0.637	

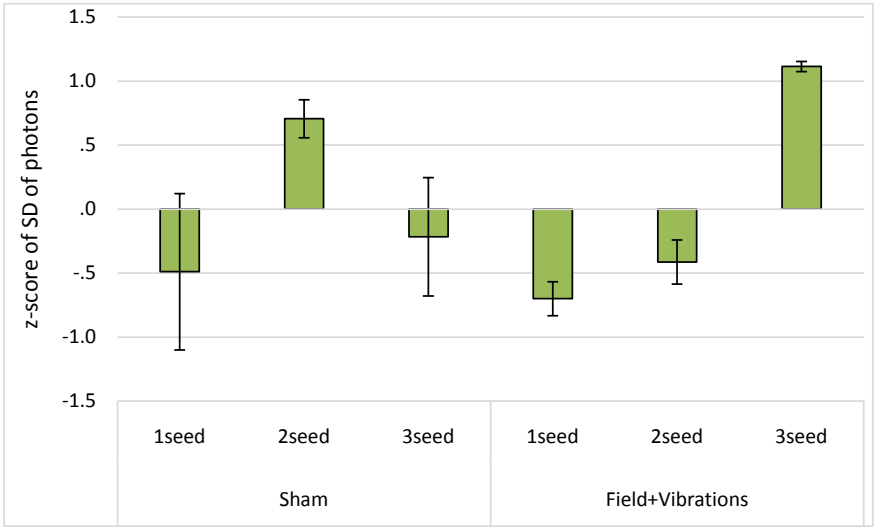

Figure 6. Z-scores of the standard deviation of recording of photon emissions per second per cm^2 (assumed diameter of 2.5 cm for PMT aperture) between the number of seeds measured each replicate. Error bars represent SEM.

the patterns of electrical activity in the brain correlated with the resonance frequencies of the Earth's magnetic field.

The interaction in photon emissions with number of seeds was evaluated with two different statistical techniques. When using residuals that had controlled for weather variables, the interaction was significant both in the mean photons and standard deviation of photon emissions over the measurement period. However, when using the within subject z-score methods, only the standard deviation interaction remained significant. This indicates that this variable demonstrated the greatest change from exposure to the dynamic condition of the Chrysalis resonator and that the changes in SD would be seen to a lesser extent in the mean values.

Photon communication in biological organisms has been demonstrated many times [17] [18]. For example, it has been found that germinating radish seeds that had been exposed to gamma irradiation could influence the germination rate of other radish seeds that had never been exposed (Kuzin & Surbenova, 1995 in [35]). Indicating a potential for seed to seed communication through photon emission; when the seed germination rate was altered, these seeds may have been influenced by nearby seeds' through biophoton emission. Biophoton signalling has been previously implicated in the start of germination [30], in this experiment, the resonator may have altered the biophoton signalling of the seeds and as a result interfered with their germination.

In the present experiment, we found altered biophoton emission, but only when three germinating seeds were measured together, and not when one or two seeds were measured. There are several phenomena that could explain this result. The first is signal to noise ratio, where all of the seeds had altered biophoton emission, but three seeds were needed for the PMT to be able to detect the difference between conditions. Another explanation for the results is that the increased photon emissions of the three seeds measured together was the result of a stress reaction in the seeds due to overcrowding. It has been previously demonstrated that changes in population density of biological organisms can alter their biophoton emission [16] and also influence the growth of organisms nearby [18] [23]. This could imply that the resonator induced the germinating seeds to be hyper sensitive to the presence of other seeds nearby. This may also explain the decrease in germination that was found, in that it was a response to increased population density, which could also explain why the decrease in germination was found 48 hours after the beginning of germination and not 24 hours after. There is an increased likelihood that the plants would be able to sense the presence of surrounding seeds at that time, either by their individual biophoton emission, physical contact or seed leachates.

5. Conclusion

This experiment demonstrated that the Chrysalis resonator can affect the germination of sunflower seeds as well as their biophoton emissions. Further re-

search needs to be conducted to find the mechanisms by which magnetic fields affect plants. Literature reviews [1] [2] have found highly variable responses of plants to magnetic fields. Here we demonstrated the importance of considering the influence environmental conditions may have on results.

Conflicts of Interest

The authors declare no conflicts of interest regarding the publication of this paper.

References

[1] Maffei, M.E. (2014) Magnetic Field Effects on Plant Growth, Development, and Evolution. *Frontiers in Plant Science*, **5**, 445. https://doi.org/10.3389/fpls.2014.00445

[2] Nyakane, N.E., Markus, E.D. and Sedibe, M.M. (2019) The Effects of Magnetic Fields on Plants Growth: A Comprehensive Review. *International Journal of Food Engineering*, **5**, 79-87.

[3] Vian, A., Davies, E., Gendraud, M. and Bonnet, P. (2016) Plant Responses to High Frequency Electromagnetic Fields. *BioMed Research International*, **2016**, Article ID: 1830262. https://doi.org/10.1155/2016/1830262

[4] Naz, A., Jamil, Y., ulHaq, Z., Iqbal, M., Ahmad, M.R., Ashraf, M.I. and Ahmad, R. (2012) Enhancement in the Germination, Growth and Yield of Okra (*Abelmoschus esculentus*) Using Pre-Sowing Magnetic Treatment of Seeds. *Indian Journal of Biochemistry and Biophysics*, **49**, 211-214.

[5] Aleman, E.I., Mbogholi, A., Boix, Y.F., Gonzalez-Ohnedo, J. and Chalfun, A. (2014) Effects of EMFs on Some Biological Parameters in Coffee Plants (*Coffea arabica* L.) Obtained by *in Vitro* Propagation. *Polish Journal of Environmental Studies*, **23**, 95-101.

[6] Mroczek-Zdyrska, M., Kornarzynski, K., Pietruszewski, S. and Gagos, M. (2016) The Effects of Low-Frequency Magnetic Field Exposure on the Growth and Biochemical Parameters in Lupin (*Lupinus angustifolius* L.). *Plant Biosystems*, **151**, 504-511. https://doi.org/10.1080/11263504.2016.1186123

[7] Belyavskaya, N.A. (2004) Biological Effects Due to Weak Magnetic Field on Plants. *Advances in Space Research*, **34**, 1566-1574. https://doi.org/10.1016/j.asr.2004.01.021

[8] Rakosy-Tican, L., Aurori, C. and Morariu, V. (2005) Influence of Near Null Magnetic Field on *in Vitro* Growth of Potato and Wild Solanum Species. *Bioelectromagnetics*, **26**, 548-557. https://doi.org/10.1002/bem.20134

[9] Namba, K., Sasao, A. and Shibusawa, S. (1995) Effect of Magnetic Field on Germination and Plant Growth. *Acta Horticulturae*, **399**, 143-148. https://doi.org/10.17660/ActaHortic.1995.399.15

[10] Betti, L., Trebbi, G., Fregola, F., Zurla, M., Mesirca, P., Brizzi, M. and Borghini, F. (2011) Weak Static and Extremely Low Frequency Magnetic Fields Affect *in Vitro* Pollen Germination. *The Scientific World Journal*, **11**, 875-890. https://doi.org/10.1100/tsw.2011.83

[11] Radhakrishnan, R. and Kumari, B.D. (2013) Influence of Pulsed Magnetic Field on Soybean (*Glycine max* L.) Seed Germination, Seedling Growth and Soil Microbial Population. *Indian Journal of Biochemistry and Biophysics*, **50**, 312-317.

[12] Huang, P., Tang, J., Feng, C., Cheng, P. and Jang, L. (2018) Influences of Extremely Low Frequency Electromagnetic Fields on Germination and Early Growth of Mung Beans. *IEEE International Conference on Consumer Electronics-Taiwan*, Taichung, 1-2. https://doi.org/10.1109/ICCE-China.2018.8448809

[13] Vashisth, A. and Nagarajan, S. (2009) Effect on Germination and Early Growth Characteristics in Sunflower (*Helianthus annus*) Seeds Exposed to Static Magnetic Field. *Journal of Plant Physiology*, **167**, 149-156. https://doi.org/10.1016/j.jplph.2009.08.011

[14] Ćirković, S., Bačić, J., Paunović, N., Popović, T.B., Trbovich, A.M., Romčević, N. and Ristić-Djurović, J.L. (2017) Influence of 340 mT Static Magnetic Field on Germination Potential and Mid-Infrared Spectrum of Wheat. *Bioelectromagnetics*, **38**, 533-540. https://doi.org/10.1002/bem.22057

[15] Podleśna, A., Bojarszczuk, J. and Podleśny, J. (2019) Effects of Pre-Sowing Magnetic Field Treatment on Some Biochemical and Physiological Processes in Faba Bean (*Vicia faba* L. spp. *Minor*). *Journal of Plant Growth Regulation*, 1-8. https://doi.org/10.1007/s00344-019-09920-1

[16] Galle, M., Neurohr, R., Altmann, G., Popp, F.A. and Nagl, W. (1991) Biophoton Emission from Daphnia Magna: A Possible Factor in the Self-Regulation of Swarming. *Experientia*, **47**, 457-460. https://doi.org/10.1007/BF01959943

[17] Albrecht-Buehler, G. (2005) A Long-Range Attraction between Aggregating 3T3 Cells Mediated by Near-Infrared Light Scattering. *Journal of Cell Biology*, **114**, 493-502. https://doi.org/10.1083/jcb.114.3.493

[18] Fels, D. (2009) Cellular Communication through Light. *PLoS ONE*, **4**, e5086. https://doi.org/10.1371/journal.pone.0005086

[19] Dotta, B.T., Saroka, K.S. and Persinger, M.A. (2012) Increased Photon Emission from the Head While Imagining Light in the Dark Is Correlated with Changes in Electroencephalographic Power: Support for Bókkon's Biophoton Hypothesis. *Neuroscience Letters*, **513**, 151-154. https://doi.org/10.1016/j.neulet.2012.02.021

[20] Persinger, M.A., Dotta, B.T., Karbowski, L.M. and Murugan, N.J. (2015) Inverse Relationship between Photon Flux Densities and Nanotesla Magnetic Fields over Cell Aggregates: Quantitative Evidence for Energetic Conservation. *FEBS Open Bio*, **5**, 413-418. https://doi.org/10.1016/j.fob.2015.04.015

[21] Dotta, B.T., Murugan, N.J., Karbowski, L.M., Lafrenie, R.M. and Persinger, M.A. (2014) Shifting Wavelengths of Ultraweak Photon Emissions from Dying Melanoma Cells: Their Chemical Enhancement and Blocking Are Predicted by Cosic's Theory of Resonant Recognition Model for Macromolecules. *Naturwissenschaften*, **101**, 87-94. https://doi.org/10.1007/s00114-013-1133-3

[22] Dotta, B.T., Karbowski, L.M., Murugan, N.J., Vares, D.A.E. and Persinger, M.A. (2016) Ultra-Weak Photon Emissions Differentiate Malignant Cells from Non-Malignant Cells *in Vitro*. *Archives in Cancer Research*, **4**, 2. https://doi.org/10.21767/2254-6081.100085

[23] Fels, D. (2017) Endogenous Physical Regulation of Population Density in the Freshwater Protozoan *Paramecium caudatum*. *Scientific Reports*, **7**, Article No. 13800. https://doi.org/10.1038/s41598-017-14231-0

[24] Bernard, B.S. and William, A. (1951) Light Production by Green Plants. *The Journal of General Physiology*, **20**, 809-820. https://doi.org/10.1085/jgp.34.6.809

[25] Yan, Y. (2006) Biophoton Emission and Delayed Luminescence of Plants. In: *Biophotonics—Optics Science and Engineering for the 21th Century*, Springer, New York, 195-204. https://doi.org/10.1007/0-387-24996-6_15

[26] Gallep, C.M. and dos Santos, S.R. (2007) Photon-Counts during Germination of Wheat (*Triticum aestivum*) in Wastewater Sediment Solutions Correlated with Seedling Growth. *Seed Science and Technology*, **35**, 607-614. https://doi.org/10.15258/sst.2007.35.3.08

[27] Sun, Y., Wang, C. and Dai, J. (2010) Biophotons as Neural Communication Signals Demonstrated by *in Situ* Biophoton Autography. *Photochemical & PhotobiologicalSciences*, **9**, 315-322. https://doi.org/10.1039/b9pp00125e

[28] Moraes, T.A., Barlow, P.W., Klingelé, E. and Gallep, C.M. (2012) Spontaneous Ultra-Weak Light Emissions from Wheat Seedlings Are Rhythmic and Synchronized with the Time Profile of the Local Gravimetric Tide. *Die Naturwissenschaften*, **99**, 465-472. https://doi.org/10.1007/s00114-012-0921-5

[29] Gallep, C.M., Moraes, T.A., Cervinková, K., Cifra, M., Katsumata, M. and Barlow, P.W. (2014) Lunisolar Tidal Synchronism with Biophoton Emission during Intercontinental Wheat-Seedling Germination Tests. *Plant Signaling & Behavior*, **9**, e28671. https://doi.org/10.4161/psb.28671

[30] Footitt, S., Palleschi, S., Fazio, E., Palomba, R., Finch-Savage, W.E. and Silvestroni, L. (2016) Ultraweak Photon Emission from the Seed Coat in Response to Temperature and Humidity—A Potential Mechanism for Environmental Signal Transduction in the Soil Seed Bank. *Photochemistry and Photobiology*, **92**, 678-687. https://doi.org/10.1111/php.12616

[31] Tessaro, L.W.E., Murugan, N.J. and Persinger, M.A. (2015) Bacterial Growth Rates Are Influenced by Cellular Characteristics of Individual Species When Immersed in Electromagnetic Fields. *Microbiological Research*, **172**, 26-33. https://doi.org/10.1016/j.micres.2014.12.008

[32] Pobachenko, S.V., Kolesnik, A.G., Borodin, A.S. and Kalyuzhin, V.V. (2006) The Contingency of Parameters of Human Encephalograms and Schumann Resonance Electromagnetic Fields Revealed in Monitoring Studies. *Biophysics*, **51**, 480-483. https://doi.org/10.1134/S0006350906030225

[33] Persinger, M.A. (2014) Schumann Resonance Frequencies Found within Quantitative Electroencephalographic Activity: Implications for Earth-Brain Interactions. *International Letters of Chemistry, Physics and Astronomy*, **30**, 24-32. https://doi.org/10.18052/www.scipress.com/ILCPA.30.24

[34] Saroka, K.S., Vares, D.E. and Persinger, M.A. (2016) Similar Spectral Power Densities within the Schumann Resonance and a Large Population of Quantitative Electroencephalographic Profiles: Supportive Evidence for Koenig and Pobachenko. *PLoS ONE*, **11**, e0146595. https://doi.org/10.1371/journal.pone.0146595

[35] Cifra, M., Fields, J.Z. and Farhadi, A. (2011) Electromagnetic Cellular Interactions. *Progress in Biophysics and Molecular Biology*, **105**, 223-246. https://doi.org/10.1016/j.pbiomolbio.2010.07.003

Scientific Research Publishing

Open Journal of Biophysics, 2019, 9, 267-275
https://www.scirp.org/journal/ojbiphy
ISSN Online: 2164-5396
ISSN Print: 2164-5388

Assessment of Radiotherapy Treatment Field on Portal Film Using Image Processing

Nouf Abuhadi[1], Ali Bakry Abdoelrahman Hassan[2]

[1]Radiology Department, College of Applied Medical Science, Jazan University, Jazan, KSA
[2]Radiotherapy Department, College of Medical Radiological Science, Sudan University of Science and Technology, Khartoum, Sudan
Email: abdoelrahmanhassan@gmail.com

How to cite this paper: Abuhadi, N. and Abdoelrahman Hassan, A.B. (2019) Assessment of Radiotherapy Treatment Field on Portal Film Using Image Processing *Open Journal of Biophysics*, **9**, 267-275.
https://doi.org/10.4236/ojbiphy.2019.94019

Received: August 10, 2019
Accepted: September 26, 2019
Published: September 29, 2019

Abstract

Many factors contribute to the accuracy of delivered dose to patients in external-beam radiotherapy (EBRT). Although some of these factors can be checked by implementing suitable quality control procedures, the main aim was to assess the radiotherapy treatment filed on portal film using image processing technique in order to increase the accuracy of treatment delivery to the tumor by measuring the actual F/S, dose uniformity and penumbra size using portal film. This research is conducted at radiation therapy department, Khartoum Oncology Center (RICK), Khartoum state, Sudan, from July-2014 up to December-2014. The field size of each type of radiotherapy Co^{60} is measured as (9.4 × 9.4) cm and (9.1 × 9.1) cm, for linear accelerator machines it was 10 × 10 cm exactly as the reference field size, and there is no area reduced in linacs. The penumbra size for the two types of Co^{60} machine was measured also and it was 1.2 cm and 1.0 cm, and penumbra size of the linear accelerator machines was found to be 4 mm. The area of the field that received radiation by 100% was measured and it was 94.1% and 91.1% in Co^{60} and 100% for linear accelerator machine and that means linacs deliver the 100% of the dose to the useful field size. The dose percentage in the field for Co^{60} was 98.0% and 94.1% and thus the dose in the border of field 83.1% and 89.0% and it's different in linacs because the dose percentage in the field was 78.4% and 78.4% and there is no measurable dose outside its field. Penumbra Co^{60} machines are relatively large which increase radiation dose to normal tissue and reduce the TCP, so calculation and accuracy of such calculation are necessary to the patient in term of NTCP.

Keywords

Films, Image Processing, Radiotherapy, RICK, Malignancy, IDL, Oncology

1. Introduction

Teletherapy cobalt-60 units were first used for patient treatment in 1951 in Canada [1] [2]. Cobalt-60 was manufactured by irradiating cobalt-59 in a high neutron flux nuclear reactor. The main reasons for its suitability for teletherapy are the availability of relatively small, high specific activity, sources that reduce the beam penumbra; its relatively long half-life (5.27 years); and the almost monochromatic high-energy photon emission (photons of 1.173 MeV and 1.333 MeV in equal quantity) [3].

Various beam collimators designs exist to give variable rectangular fields with sides ranging in length, typically, from 4 cm to 30 cm or even up to 40 cm on isocentric units with a source axis distance (SAD) of 100 cm. Each of the four collimator leaves is usually focused on the edge of the source proximal to it, so as to avoid cut-off of the primary beam and minimize penumbra. Distances from the source to the far edge of the collimators are typically between 40 cm and 50 cm for machines designed for 80 cm SSD, but this distance may be increased by penumbra trimmers that are particularly desirable when the machine is to be used for 100 cm SSD treatment [3].

Field Size: can be defined as the measure of an area irradiated by a given beam; there are two most useful conventions. The first is the geometric field size; The geometric projection on a plane perpendicular to the central ray of the distal end of the collimator is as seen from the center of the front surface of the source. The second is the physical field size, defined as the area included within the 50 percent maximum dose isodose curve at the depth of maximum dose [4].

While the ***Penumbra size***: The penumbra for electron beams is defined either in terms of the distance between two isodose values on a beam profile at the depth of maximum dose (or at the standard measurement depth), or indirectly in terms of distances between specified isodose and the geometric field edge under stated conditions as above. If the former, then generally the 20% - 80% width is expected to be 10 mm to 12 mm for electron beams below 10 MeV, and 8 mm to 10 mm for electron beams between 10 MeV and 20 MeV. These values apply for applicators with the final collimation stage at 5 cm or less from the skin, but for greater separation between the applicator and the skin the penumbra will increase. With careful design of the collimation system and a 15 mm diameter source, a penumbra of no more than 10 mm (distance between the 20% and 80% decrement lines) may be achieved at 5 cm depth for field sizes with an area of less than 400 cm^2 [3].

The process of image manipulation in medical imaging was recently introduced as a very important issue in case of image processing; in this case we used this disciplines in case of calculating and accurately identifying the penumbra profile rather than using of conventional method such as QA programs and portal film in collaborations with treatment machine.

Linear accelerator is considering to have very excellent geometrical accuracy when it compared with Co^{60} machine and the presence of penumbra is relatively

large in Co^{60} and it depend on the source size, depth, SDD and source diaphragm distance [4]. This research aimed to answer important questions which are; is it possible to have best assessment of radiotherapy treatment field? Does this method give the exact determination of radiation field size and penumbra size? Does this method give the correct value of uniformity?

2. Review of Literature

[5] stated that the field size that calculated by computerized score using Matlab program was 9.9 ± 0.36049 cm × 9.9 ± 0.1123 cm calculated form digitized film. [6], aimed to verify radiotherapy treatments: computerized analysis of the size and shape of radiation fields using portal imaging. [7] studied the high energy linear accelerator penumbra size using the Pencil Beam Convolution algorithms and self-developing Gafchromic™ EBT2 film, he found that increased energy, field size and depth rise to an increased penumbra (20% - 80%) width. For a 6 MV photon energy, the penumbra widths (20% - 80%) at 1.5 cm, 5 cm, and 10 cm depths were 4.2 mm, 4.4 mm, and 5.7 mm for the eclipse calculations and 2.9 mm, 4.1 mm, and 4.2 mm for the EBT2 film measurements for 10 × 10 cm field sizes, respectively.

3. Materials and Methods

This study conducted at radiation oncology center (RICK) to assess the radiation filed size uniformity and calculating the penumbra profile. radiographic images with Linear accelerator machine (ELECTA) 10 Mv, and two types of cobalt-60 machines Co-60 1) EQUINOX source size 2.5 × 1.5 × 1.5 cm Active size 1 × 1 × 1 cm and the second type Co-60 2) MDS source size 1 × 1 × 1 cm, 0.75 × 0.75 × 0.75 cm, with Focus 1 cm; performed using the verification film subjectively by placing a ready pack direct exposure film on the table on the SAD. With the collimator angle set at 0˚, 10 × 10 cm square light fields obtained and the edges marked with a radiopaque object or a ballpoint pen by drawing lines on the film jacket with sufficient pressure to scratch the emulsion. Then the film was exposed for 1 - 2 min to obtain an optical density in the linear range of its sensitometric curve, usually around (1). Two more exposures at the collimator angles of +90˚ were made using fresh area of the same film or another film. The film processed in an automatic rapid processor. With millimeter graph paper attached to the patient treatment table raised to the nominal isocenter distance, the gantry was orientated to point the collimator axis of rotation vertically downward. Radiographic film to obtain an optimal radiographic density according to usable factor in all machines. Illustrating the 10 × 10 cm field size, and two regions of penumbra, and the percentage of the dose in the field, in addition do dose uniformity was assessed. Each film scanned using digitizer scanner then treated by using image processing program (IDL) after converting the images into TIFF format as IDL input variable, where the field size and penumbra and the uniformity of radio therapy beam will be determined, accelerator for

vertical and horizontal reading on The portal films, with SSD = 100 cm and the field size 10 × 10 cm^2 and isocentric set-up 0, 90, 180, and 270 degrees, and the variables used to achieve these results. Aline were drowning through the images and line histogram was obtained in order to calculate the frequency of intensity difference throughout the (the line) filed. And the result showed that (Figure 1):

Figure 1. Illustration of Co^{60} machine.

4. Result (Tables 1-4, Figure 2 & Figure 3)

Table 1. Measured field size and the percentage of the radiation received for all machines.

Machine	*Reference Filed* (10 × 10) *cm*	*%*
Co^{60}	9.41766 × 9.41766 cm	94.2%
Co^{60}	9.11417 × 9.11417 cm	91.142%
Linear	10.0 × 10.0 cm	100%
Linear	10.0 × 10.0 cm	100%

Table 2. Area reduced from reference field size.

Machine	Reduced area from the field size
Co^{60}	0.58234 cm
Co^{60}	0.88583 cm
Linear	0.0000
Linear	0.0000

Table 3. Percentage of the field received radiation by 100%.

Machine	Dose percentage in the field	Dose percentage in the border of the field
Co^{60}	98.039 %	83.137%
Co^{60}	94.118 %	89.02%
Linear	78.431%	-
Linear	78.431%	-

Table 4. Penumbra size.

Machine	Penumbra size
Co^{60}	1.224
Co^{60}	1.0363
Linear	0.4517
Linear	0.4637

(*Note: the figures presented here it's an example from one cobalt and one linear just*)

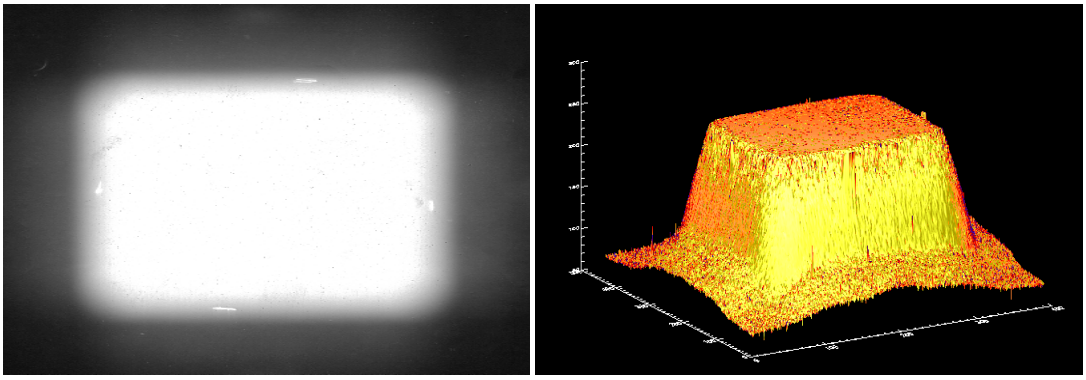

(a) (b)

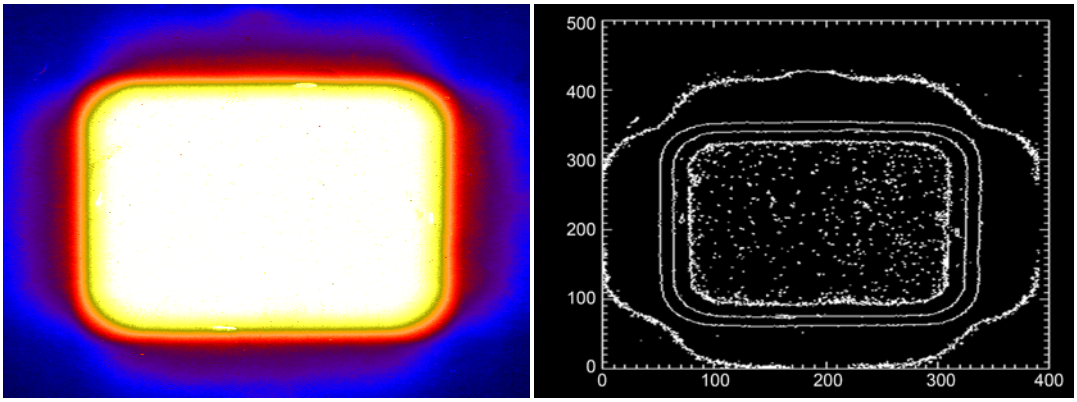

(c) (d)

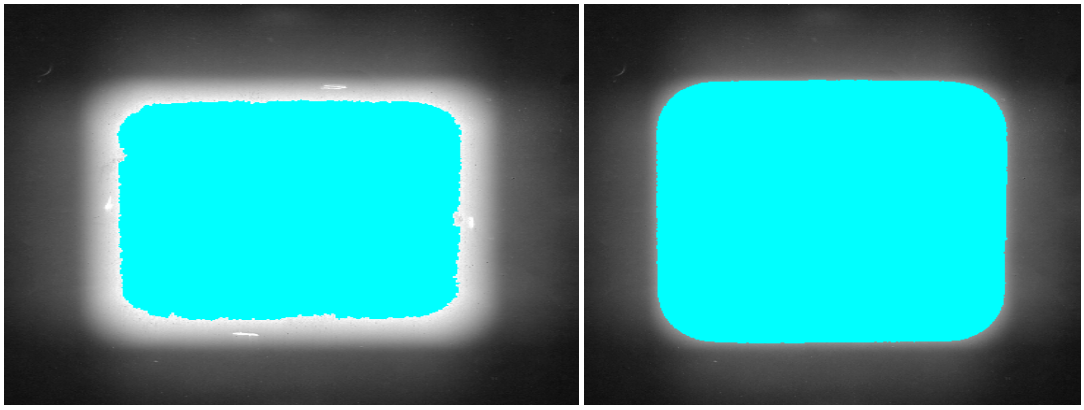

(e) (f)

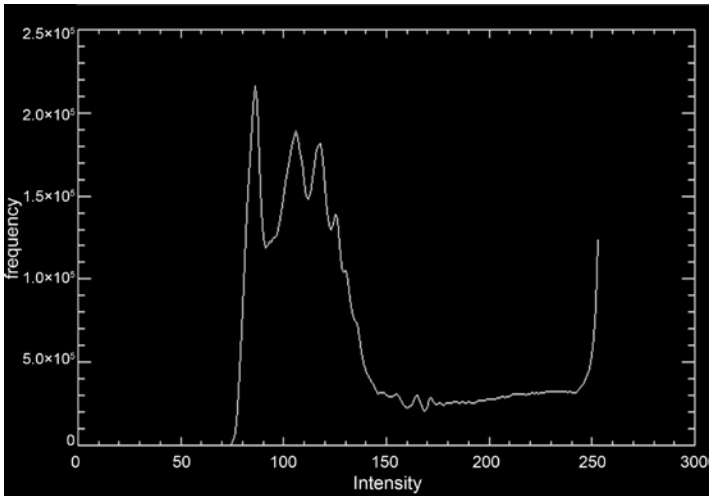

(g)

Figure 2. (a) Radiographic image with Co-60, Measured field size was 9.41766 × 9.41766 cm, 94.1766 %; (b) Histogram showing the reduced area from the reference field size in Co-60 machine and it was 0.58234 cm; (c) Field size 9.41766 × 9.41766 cm, 94.1766% with white color, border of the field with yellow and penumbra region 1.224 cm with orange and red color; (d) Contour for the image; (e) Percentage of the dose in the field was 98.039% and in the border 83.137% for Co-60 machine; (f) The field size 10 × 10 cm; (g) Histogram showing scatter and penumbra region.

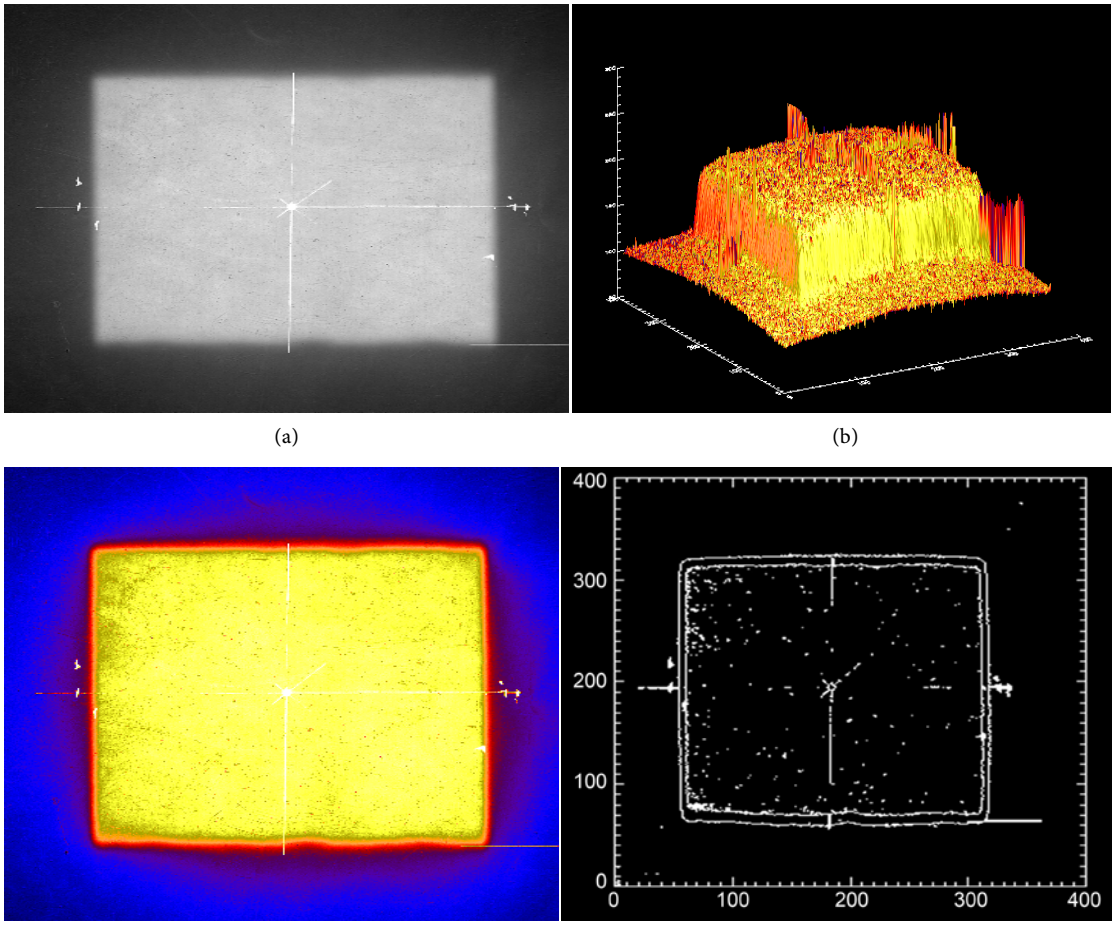

(a) (b)

(c) (d)

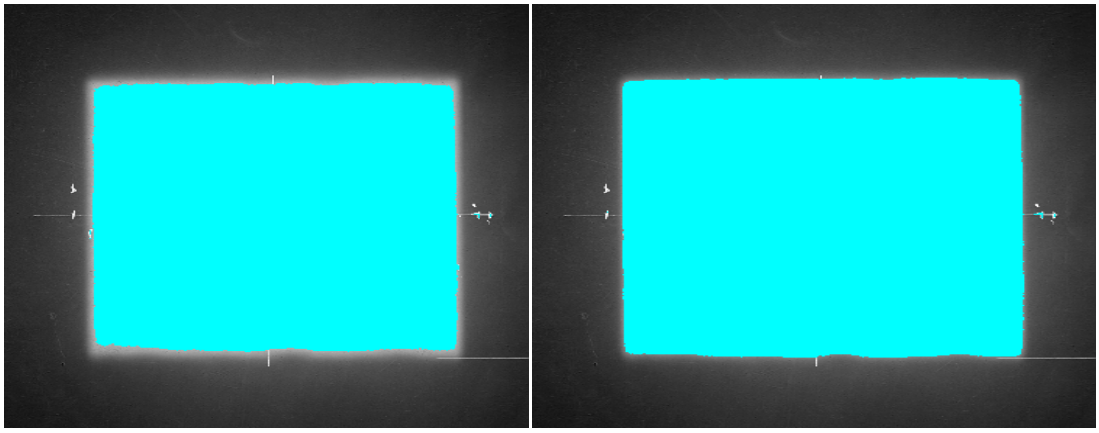

(e) (f)

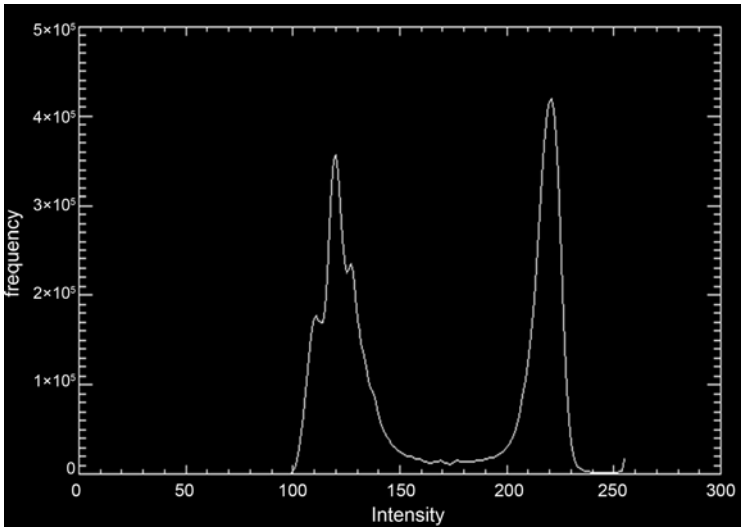

(g)

Figure 3. (a) Radiographic image with linear accelerator measured field size was 10 × 10; (b) Histogram showing the reduced area from the reference field size for linear accelerator. Machine and it was 0.000 cm; (c) Useful field size 10 × 10 cm with white color, border of the field with yellow and penumbra region 0.4517 with orange and red color; (d) Contour for the image; (e) Percentage of the dose in the field was 78.431% and in the border 0.000%. For linear accelerator machine; (f) The size 10 × 10 cm; (g) Histogram showing scatter and penumbra region.

5. Discussion

This study performed to assess the radiotherapy beam by measuring the field size, penumbra size and the percentage of the field dose, the results of these study showed that the field size of two type of Co^{60} machine was (9.4 × 9.4) cm and (9.1 × 9.1) cm as in Table 1. For each Co-^{60}, the reduction in field size was 0.58234 cm (as Figure 2(b) in first type and 0.88583 cm (see Table 2) in the second one and its means that the verification light and field size doesn't matched and that due to adjustment error in the machine (mechanical error), for linear accelerator machines the field size was measured to be 10 × 10 cm (Table 1) exactly as the reference field size, and there is no area reduced in linacs. Figure 3, Table 2.

The penumbra size for the two types of Co-^{60} machine was measured also as

Garduñ *et al.* 2007, and Se An Oh *et al.*, [7] studies, and it was 1.224 cm (**Figure 2(c)**) and 1.0363 cm, and the penumbra size of the linear accelerator machines was found to be 0.4637 cm and 0.4517 cm (**Table 4**) as [8]. This difference in the size of the penumbra is totally clear as in **Table 4**. Where the cobalt penumbra size was more than 1 cm but less than 0.5 cm in Linear accelerator, this overexpansion of the field can lead to excessive irradiation of normal tissue around the estimated field size for any kind of treatment and for any filed size, so in Co-60 can be manipulated according to the source size and acceptable activity required for treatment, the use of trimmer or half beam block may be helpful in Co-60. Also QC program in required time schedule should be carefully done.

The area of the field that received radiation by 100% as [9] study was measured and it was 94.1% and 91.1% in Co^{60} and 100% for linear accelerator machine and that means linacs. Machines deliver 100% of the dose to the useful field size. The dose percentage in the field for Co-60 was 98.0% and 94.1% and thus the dose in the border of field 83.1% and 89.0% and it's different in linacs because the dose percentage in the field was 78.431% and 78.431% and there is no measurable dose outside the field size of linacs. As in **Figure 3(e)** (**Table 3**).

6. Conclusions

The process of treatment using high energy of radiation carries a great risk for normal tissue damage, where high quality of radiation is used.

Penumbra is unwanted projectile distance at the edge of the beam which is harmful to normal tissue around the FS. This study reveals that CO^{60} machine has a large size of penumbra rather than the linear accelerator should be considered in treatment carrying a great amount of normal tissue or low tolerance to radiation.

This study concludes that linear accelerator is more precise than Co^{60} in term of lateral distance from the edge of the field. Also using the image processing program is more accurate in estimation of dose uniformity and linearity that the conventional portal film method, where the distance is measured randomly, can represent these measured values numerically and graphically.

Conflicts of Interest

The authors declare no conflicts of interest regarding the publication of this paper.

References

[1] Green, D.T. and Ferrington, R.F. (1952) 1000 Curie Cobalt Units for Radiation Therapy. III. Design of a Cobalt 60 Beam Therapy Unit. *British Institute of Radiology*, **25**, 309-313. https://doi.org/10.1259/0007-1285-25-294-309

[2] Johns, H., *et al.* (1951) 1,000-Curie Cobalt-60 Units for Radiation Therapy. *Nature*, **168**, 1035.

[3] Mayles, P., Nahum, A.E. and Rosenwald, J.-C. (2007) Handbook of Radiotherapy Physics: Theory and Practice. CRC Press, Boca Raton.

https://doi.org/10.1201/9781420012026

[4] Khan, F.M. and Gibbons, J.P. (2014) Khan's the Physics of Radiation Therapy. Lippincott Williams & Wilkins, Philadelphia.

[5] Abdallah, Y.M. and Boshara, M.A. (2014) Assessment of Field Size on Radiotherapy Machines Using Texture Analysis. *Sudan Medical Monitor*, **9**, 5. https://doi.org/10.4103/1858-5000.144642

[6] Leszczynski, K.W., Shalev, S. and Gluhchev, G. (1993) Verification of Radiotherapy Treatments: Computerized Analysis of the Size and Shape of Radiation Fields. *Medical Physics*, **20**, 687-694. https://doi.org/10.1118/1.597017

[7] Oh, S.A., *et al.* (2012) Study of the Penumbra for High-Energy Photon Beams with Gafchromic™ EBT2 Films. *Journal of the Korean Physical Society*, **60**, 1973-1976. https://doi.org/10.3938/jkps.60.1973

[8] Cheung, T., Butson, M.J. and Yu, P.K. (2006) Measurement of High Energy X-Ray Beam Penumbra with Gafchromic™ EBT Radiochromic Film. *Medical Physics*, **33**, 2912-2914. https://doi.org/10.1118/1.2218318

[9] Kron, T., Elliott, A. and Metcalfe, P. (1993) The Penumbra of a 6-MV X-Ray Beam as Measured by Thermoluminescent Dosimetry and Evaluated Using an Inverse Square Root Function. *Medical Physics*, **20**, 1429-1438. https://doi.org/10.1118/1.597157

Call for Papers

Open Journal of Biophysics

ISSN Print: 2164-5388 ISSN Online: 2164-5396
https://www.scirp.org/journal/ojbiphy

Open Journal of Biophysics (OJBIPHY) is an international journal dedicated to the latest advancement of biophysics. The goal of this journal is to provide a platform for scientists and academicians all over the world to promote, share, and discuss various new issues and developments in different areas of biophysics.

Subject Coverage

All manuscripts must be prepared in English, and are subject to a rigorous and fair peer-review process. Accepted papers will immediately appear online followed by printed hard copy. The journal publishes original papers including but not limited to the following fields:

- Bioelectromagnetics
- Bioenergetics
- Bioinformatics and Computational Biophysics
- Biological Imaging
- Biomedical Imaging and Bioengineering
- Biophysics of Disease
- Biophysics of Photosynthesis
- Cardiovascular Biophysics
- Cell Biophysics
- Medical Biophysics
- Membrane Biophysics
- Molecular Biophysics and Structural Biology
- Physical Methods
- Physiology and Biophysics of the Inner Ear
- Proteins and Nucleic Acids Biophysics
- Radiobiology
- Receptors and Ionic Channels Biophysics
- Sensory Biophysics and Neurophysiology
- Systems Biophysics
- Theoretical and Mathematical Biophysics

We are also interested in: 1) Short Reports—2-5 page papers where an author can either present an idea with theoretical background but has not yet completed the research needed for a complete paper or preliminary data; 2) Book Reviews—Comments and critiques.

Notes for Intending Authors

Submitted papers should not have been previously published nor be currently under consideration for publication elsewhere. Paper submission will be handled electronically through the website. All papers are refereed through a peer review process. For more details about the submissions, please access the website.

Website and E-Mail

https://www.scirp.org/journal/ojbiphy **E-mail: ojbiphy@scirp.org**

What is SCIRP?

Scientific Research Publishing (SCIRP) is one of the largest Open Access journal publishers. It is currently publishing more than 200 open access, online, peer-reviewed journals covering a wide range of academic disciplines. SCIRP serves the worldwide academic communities and contributes to the progress and application of science with its publication.

What is Open Access?

All original research papers published by SCIRP are made freely and permanently accessible online immediately upon publication. To be able to provide open access journals, SCIRP defrays operation costs from authors and subscription charges only for its printed version. Open access publishing allows an immediate, worldwide, barrier-free, open access to the full text of research papers, which is in the best interests of the scientific community.

- High visibility for maximum global exposure with open access publishing model
- Rigorous peer review of research papers
- Prompt faster publication with less cost
- Guaranteed targeted, multidisciplinary audience

Scientific Research Publishing

Website: https://www.scirp.org

Subscription: sub@scirp.org

Advertisement: service@scirp.org